Petrophysical properties in faulted basement rocks: Insights from outcropping analogues on the West European Rift shoulders

Lionel Bertrand, Yves Géraud, Marc Diraison

Petrophysical properties in faulted basement rocks: Insights from outcropping analogues on the West European Rift shoulders.

Lionel Bertrand[a] (corresponding author) lionel.bertrand@enerex.fr ; Phone +33 3 72 74 46 57.
Yves Géraud[b], Marc Diraison[b]

[a] Enerex, 2 rue du Doyen Marcel Roubault, Vandoeuvre-les-Nancy, France.
[b] Université de Lorraine, CNRS, GeoRessources, F-54000 Nancy, France

Abstract

In continental extension settings like the West European Rift, the main target for high-temperature geothermal drillings is the fault zones in basement rocks of the grabens. However, the reservoir properties of these structures remain almost unknown during the predrilling resource evaluations. This study shows the petrophysical evolution in fault zones on three outcropping areas at the basins' shoulders. We highlight three petrographical groups with different petrophysical evolution in the fault zones: granites and granodiorites, metamorphic rocks with schistosity, and massive metamorphic or magmatic facies. It provides a first estimation of their reservoir properties that can be used for dual-porosity modeling.

Keywords

Outcrop analogue, petrophysical properties, basement rocks, fault zone

Highlights

- The properties evolution depends on mineral alteration vs microcracking process.
- For granites, petrophysical properties are in agreement with URG deep wells data.
- The weathered layer at the sedimentary/basement interface is also characterized.

1. Introduction

High enthalpy geothermal heat production is commonly located in active rifts or in subduction related magmatic arcs (*Wilmarth and Stimac, 2015*). In these geological contexts, active magmatic systems produce very high geothermal gradients that favor the installation of such energy production units. However, high geothermal gradients are also found in non-magmatic active systems, namely in extension related tectonic systems such as in the Cenozoic grabens related to the West European Rift system (WER) (Figure 1) (*Boissavy et al., 2019*). For electricity production, a fluid temperature above 150°C is required. In these grabens, with a mean geothermal gradient of around 4-5°C/100 m (*Baillieux, 2012; Freymark et al., 2017*) and common pre/syn-rift sediment thicknesses of 2-4 km (*Brun et al., 1992; Genter et al., 2004*), the drilling projects mostly target their basements. These rocks are essentially composed of sediments and magmatic rocks metamorphosed at various degrees during the pre-rift geological history.

In this type of rock, the permeability and porosity are generally low, except in fault zones where fracturing and mineral dissolution/recrystallization linked to the faulting process occurs, or in the paleo-weathered top of the basement in saprolite or fissured horizons if they are preserved when buried in the basins (Areshev et al., 1992; Nelson, 2001; Dewandel et al., 2006; Faulkner et al., 2010; Koning, 2013; Trice, 2014; Gutmanis et al., 2015). Therefore, the combination of fracture network characterization and matrix evolution properties are key outcomes for evaluation and modelling of the suitability of drilling projects (Caine et al., 1996; Bense et al., 2013). Unfortunately, there is a lack of data concerning these properties. In particular, they are linked to three main factors in the WER: 1) The high variability of rock facies in the basement associated to the structural inheritance of basement rocks, 2) the lack of boreholes crosscutting these units regarding this high facies variability, 3) the current predrilling geophysical investigation methods that poorly detect the weathered layer on top basement or the precise fault zone architecture, particularly at great depth, due to their sub-seismic dimension (*Slightam, 2014; Khair et al., 2015; Carpentier et al., 2016*).

In this paper, we use outcropping analogues of the basement formations at the shoulders of the rift to enhance knowledge about the petrophysical variation in fault zones. Thus, main rocks facies are sampled in three areas where drilling projects are currently being studied:

1) The Northern Vosges Mountains as analogues of the basement rocks in the central part of the Upper Rhine Graben (a, Figure 1).
2) The Eastern part of the French Massif Central (FMC) at the shoulders of the Valence trench (b, Figure 1).
3) Both sides of the Limagne graben in the French Massif Central (c, Figure 1).

The aim of this paper is to present the evolution of petrographic and petrophysical properties of the different basement rock facies from the undeformed rocks in the protolith to the damaged zones and fault cores, and also in the weathered layer preserved from the actual erosion. For this purpose, the mineral alteration and microcrack density were characterized with the help of thin section studies, and the sample porosity, bulk and skeletal densities, apparent permeability, P-wave velocity and thermal conductivity were measured to constrain petrographic and petrophysical evolutions. These data sets will allow the definition of petrophysical groups, and properties' evolution in fault zones for magmatic rocks but also metamorphic facies where petrophysical properties are poorly documented in the literature. Our properties

evolution models will also be compared to the few data about boreholes existing in the Upper Rhine Graben where some information exists about the fault and fracture system (*e.g. Bertrand et al., 2018*) and the alteration in the targeted fault zones (*e.g. Géraud et al., 2010; Ledésert et al., 2010; Glaas et al., 2018*), as there is a lack of data for the basement rocks in the two other studied areas (*Debrand-Passard, 1984; Genter et al., 2003*).

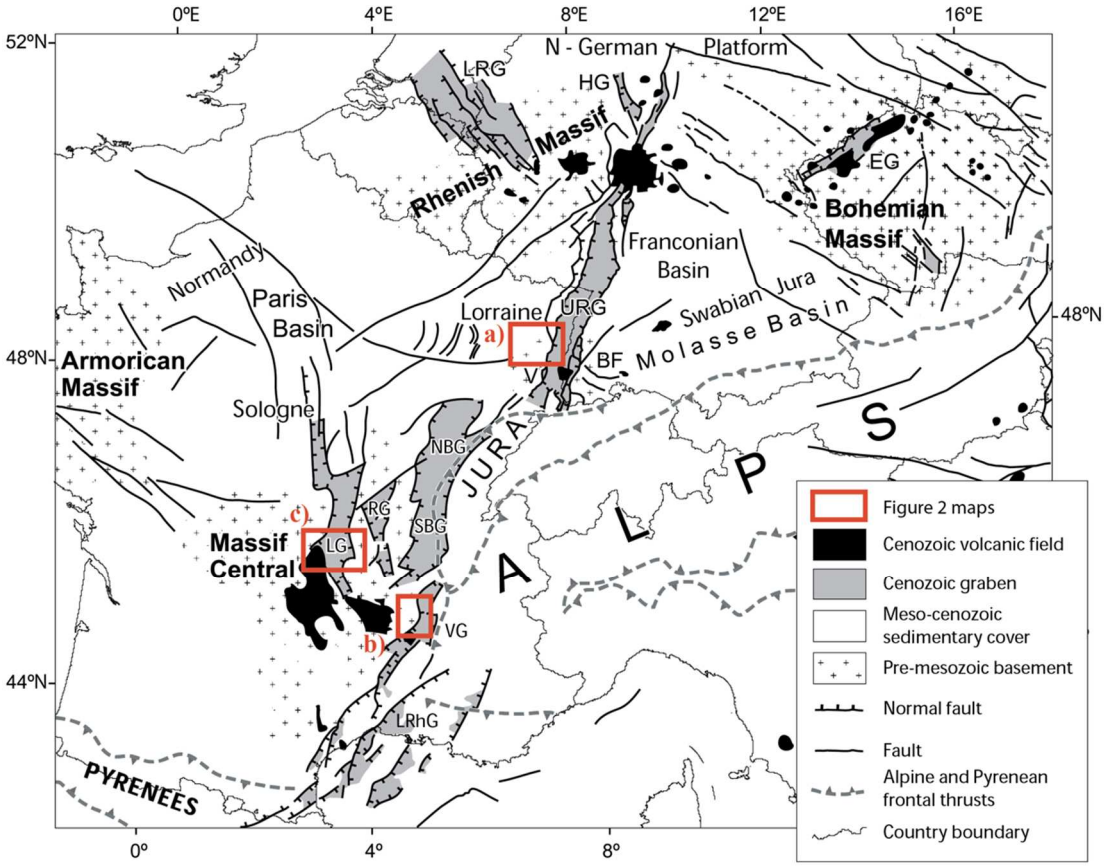

Figure 1: General map of the WER grabens with the three areas of interest of the study : a) Northern Vosges, b) Southeastern French Massif Central and c) Limagne graben's shoulders. Modified after Bourgeois et al. (2007), URG & LRG: Upper & Lower Rhine Graben, NBG & SBG: Northern & Southern Bresse Graben, RG: Roanne Graben, VG: Valence Graben, LRhG: Lower Rhône Grabens, HG: Hessian grabens, EG: Eger Graben V: Vosges and BF: Black Forest.

2. Geological settings

The overall basement of the WER-related grabens is composed of different lithotectonic domains stuck together during the large-scale Hercynian orogeny of the Paleozoic Era until 300 Ma (*Matte, 2001; Nance et al., 2010; Lardeaux et al., 2014*). Since the end of the Hercynian orogeny and the collapse of the Mountain belts in the Carboniferous and Permian periods, these lithotectonic domains are subjected to several tectonic events that reactivate the primary structures (*Schumacher, 2002; Ziegler et al., 2006).* The timing and influence of each event depends on the location and precise effect on the fault network that is not clearly constrained. Thus, it can be cited: The Triassic and Jurassic Periods of extension in the Alpine domains, and the following collision between the European and African plates with the linked Alpine

and Pyrenean orogeny (*Guillocheau et al., 2000; Sissingh, 2001; Bourquin et al., 2006*); the opening of the North Atlantic ocean during the Cretaceous Period (*Srivastava et al., 1990; Olivet, 1996*); and finally the WER tectonics from the end of the Eocene until the Pliocene Epochs for the main deformation phases (*Roussé, 2006; Bourgeois et al., 2007; Edel et al., 2007).*

Concerning the hercynian lithotectonic domains, the different rock facies in each area studied are described below.

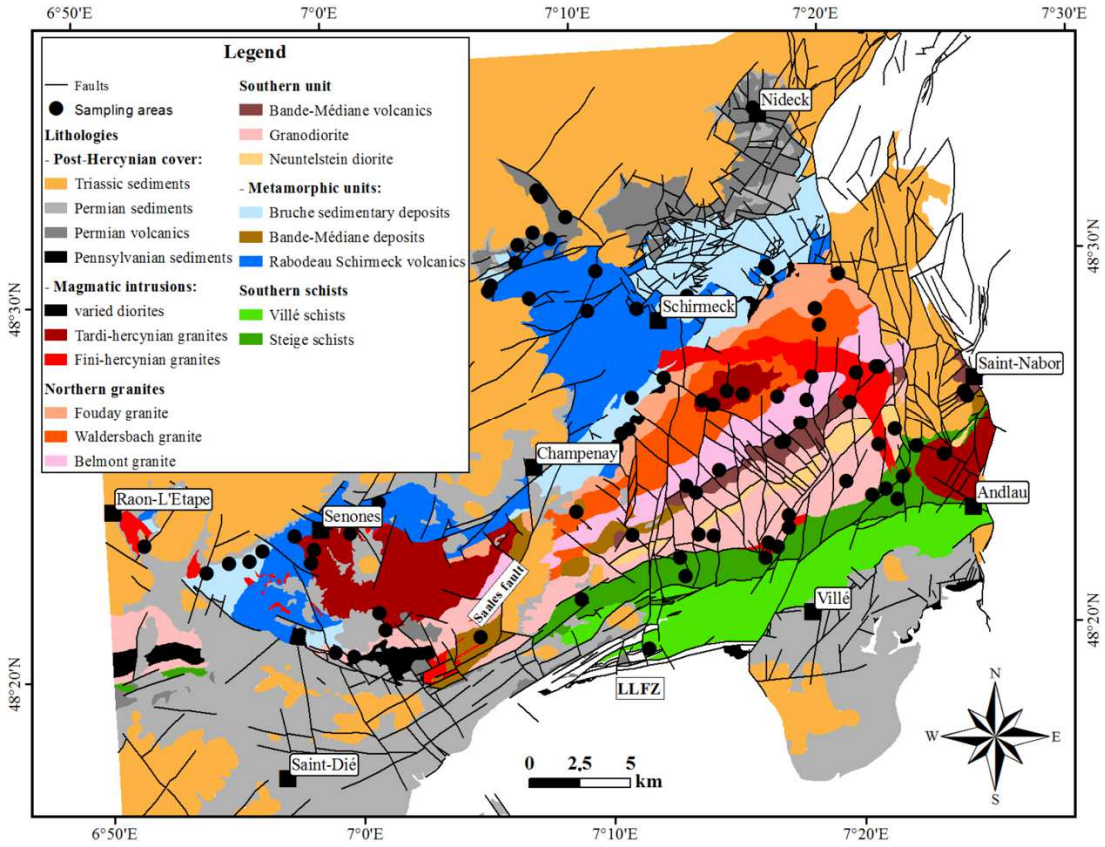

Figure 2: Geological map of the studied area in the Northern Vosges with sampling points, redrawn after Blanalt et al. (1972), Theobald et al. (1975), von Eller et al. (1975), Menillet et al. (1978) and Elsass et al. (2008).

2.1. The Northern Vosges (V)

The Northern Vosges are composed of a succession of E-W to ENE-WSW trending lithological bends (Figure 2). The Lalaye-Lubine Fault Zone (LLFZ) separates them from the Moldanubian domain, which represents the crustal root of the orogeny at the South. The affiliation of these bends to lithotectonic domains is still debated, but recent studies have emphasized a subdivision into three main units (*Tabaud et al., 2014; Skrzypek et al., 2014*):

- The northern series:

The northern part of the basement rock is a part of the Saxothuringian domain, composed of a succession of varied sedimentary rocks (Bruche unit) and volcanic intruded rocks (Rabodeau Schirmeck massif). These units were put in place from the Lower to late Upper Devonian periods and are composed of varied facies of detrital sediments with conglomerates, sandstones, pelitic and radiolarites deposits with

sparse carbonates lenses. (*Elsass et al., 2008, Skrzypek et al., 2014*). The volcanic intrusions are bimodal, with basaltic and rhyolitic lava flows. Upper Visean volcano-sedimentary succession is also preserved in the plutonic massif as the "Bande-Mediane" volcano-sedimentary unit (*Elsass et al., 2008*). Due to the collision between Saxothuringian and Teplá-Barrandian domains, the whole series are metamorphosed under anchizonal conditions (*Skrzypek., 2011*).

- The southern schists:

Along the LLFZ, the Steige and Villé schists are presumed to represent the western termination of the Teplá-Barrandian domain (*Skrzypek et al., 2014*). These are composed roughly of pelitic sediments and tuff intercalations dated in the Cambro-Ordovician periods. The Villé schists are metamorphosed under greenschists-facies conditions, while the Steige schists show a low-grade metamorphic overprint and also contact-metamorphism at the border with the plutonic massif.

- The "Champ-du-Feu" massif:

The interface between the two previous domains is encroached by the "Champ-du-Feu" massif, a Mid German Crystalline Rise type intrusion (*Tabaud, 2012*). This massif is composed of a series of NE-SW to E-W trending plutons : 1) The southern units are composed of the "Bande-Médiane" volcanics, the Neuntelstein diorites, and the Hohwald and Champ-du-Feu granodiorites bands, dated 334 ± 5 Ma for the oldest intrusion (*Cocherie, 2007; Elsass et al., 2008*); 2) The northern unit is composed of three granitic bodies: "Belmont", "Waldersbach" and "Fouday" granitic bands, dated 319 ±3 Ma (*Cocherie, 2007*). They are followed by sub-circular bodies called Tardi-Hercynian (Tardi-H) granites with from West to East the Senones, the Natzwiller and the Andlau granites (Figure 2). A later magmatic event is represented by the Kagenfels granite dated at 299 ± 7 Ma (*Boutin et al., 1995*) and some smaller bodies (Saint-Blaise, Kreuzweg, etc.), mark the end of the plutonism and are called Fini-Hercynian (Fini-H) granites. Several small dioritic plutons called "Muckenbach-type" plutons intrude into the contact of the northern suite and the Saxothuringian unit, but dating of the former is uncertain in this magmatic evolution.

2.2. The Southeastern French Massif Central (FMC)

Overall, the FMC is attached to the Moldanubian domain via a stack of six tectono-metamorphic units (*Faure et al., 2009; Lardeaux et al., 2014*). In this study, we focus on three of these that outcrops between the Southeastern border in front of the Valence trench and the large-scale Velay Migmatites dome (Figure 3):

- The Upper Gneiss Unit (UGU) is formed by Cambro-Ordovician rocks that were subjected to High-Ultra High pressure metamorphism during the Lower Devonian epoch and are represented by gneiss with various layer thicknesses, which outcrop in the "Alboussière" synform (*Faure et al. 2008).*
- The Lower Gneiss Unit (LGU) also has a Cambro-Ordovician protolith age, with metamorphism until the amphibolite facies and partial melting in the Carboniferous Period, followed by a barrovian-type metamorphism with a variable timing trough, the FMC (*Burg et al. 1984; 1989*). In the domain, this unit outcrops at the NW flank of the "La Voulte-sur-Rhone fault" and in the "Bruzac" Fold and are composed mainly of schist and mica-rich (muscovite-chlorite) schists, and some gneiss (Figure 2*b*) (*Bornand et al., 1977*).

- Two granitic bodies belong to the Carboniferous Period magmatism event that is a precursor to the Velay migmatitic dome emplacement (*Ledru et al., 2001)*. The first one has Calc-alkaline affinity and is dated at 337± 13 Ma. The second one crosscuts the first granitic body and has a Leucogranite composition with biotite and muscovite and a reduced grain size.

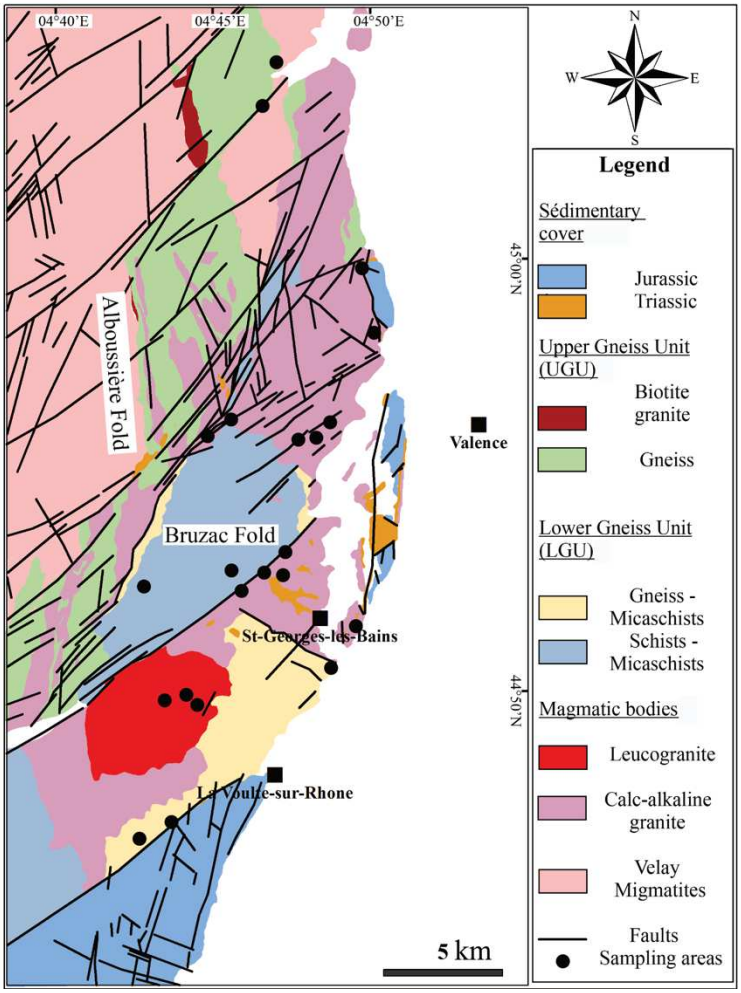

Figure 3: Geological map of the studied area in the southeastern French Massif Central (FMC) with sampling points, redrawn after Chenevoy et al. (1976), Gros et al. (1977) and Monjuvent et al. (1979).

2.3. The French Massif Central at the Limagne graben's Shoulders (L).

In the area studied at the Limagne graben shoulders, the UGU outcrops at the western shoulder and are composed of gneiss and anatexites (*Faure et al., 2002; 2009*). The Royat biotite-monzonitique granites and diorites with hornblende and biotite surround them (Figure 4).

In the Northern part, the "Tufs antracifères series" are volcano-sedimentary undeformed units that overlie the others and are dated as Late Visean (*Bruguier et al., 1998*). They are composed of sandstones, conglomerates and coal layers intercalated by felsic magmatism, mainly dacites and rhyolites.

In the Eastern and Southern part of the area, several magmatic bodies were emplaced during the Carboniferous Period:

1) The Early carboniferous granites with Chateau-Gaillard monzonitique, biotite granite and the L'Hermitage muscovite-rich leucogranite dated at 337 Ma (*Faure et al., 2002*).

2) The "red granites" represented by the "Bois Noirs" monzogranite are characterized by a low ferromagnesian mineral content and the Mayet-de-Montagne with biotite and amphibole dated to 340-330 Ma. (*Faure et al., 2002*).

3) The younger granites with muscovite Saint-Dier and Thier microgranites dated as emplaced at 320 Ma and the two-micas migmatite attached to the late-Hercynian migmatization Velay event dated between 310 and 290 Ma (*Lardeaux et al., 2014*).

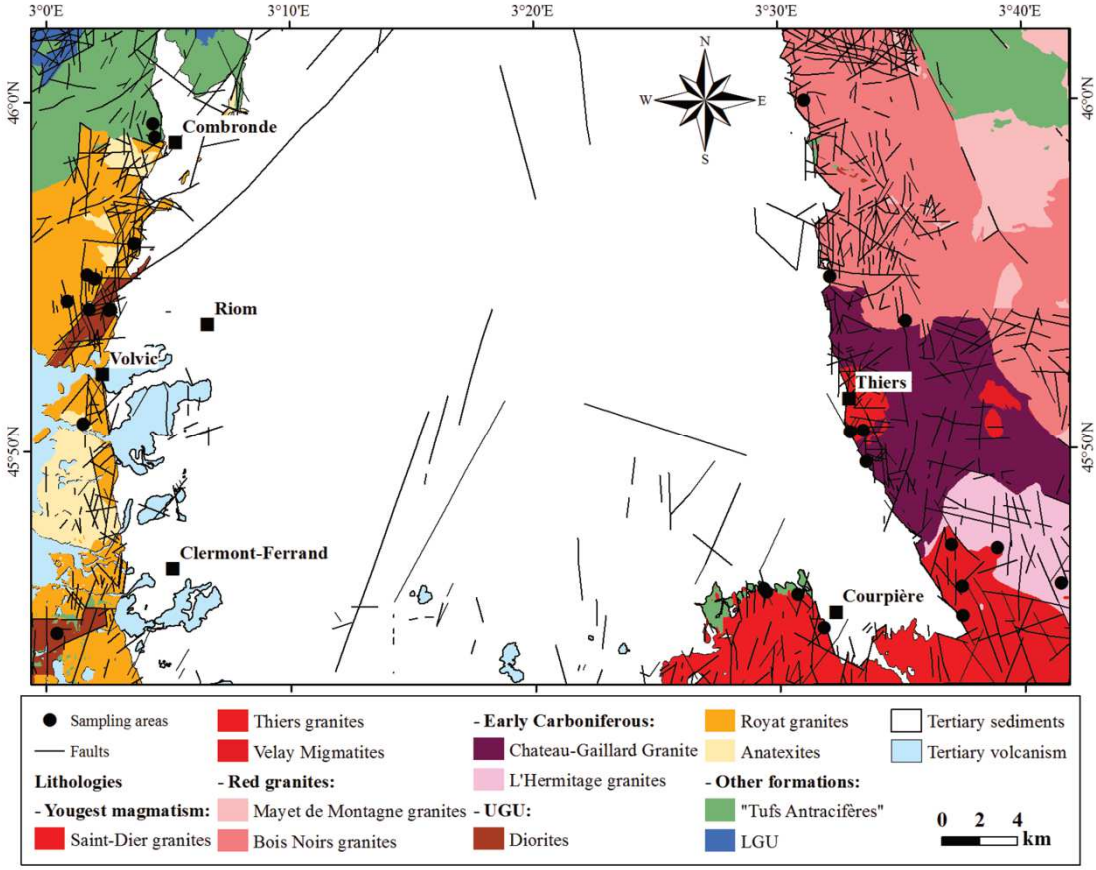

Figure 4: Geological map of the studied area in French Massif Central at the Limagne graben's Shoulders (L) with sampling points, redrawn after Jeambrun et al. (1973), Bouiller et al. (1976, 1978), Dadet et al. (1980), Giot et al. (1986), Barbarin et al. (1988).

3. Measurement methods

As the Hercynian rocks have highly heterogeneous textures and compositions, extensive sampling of all outcropping rock types was done in all three areas. Except for some carries and recent road borders, the outcropping conditions are generally too bad to take samples in their precise structural positions with respect to the fault zones. Bertrand et al. (2018) defined semi-quantitative fracture densities for metamorphic and granitic basement rocks in the Northern Vosges area. Based on this work, we chose to sample the different rock facies in light of the qualitative fracture density on the outcrop and thereafter the alteration degree. Fresh and altered samples were

206 therefore taken in fractured areas (A, Figure 5a). Few fault cores could be sampled in
207 some facies, and these were mostly represented by incohesive breccias or cataclasis or
208 highly fractured corridors (B & C, Figure 5a). When the outcropping conditions were
209 appropriate (not too much actual weathering, enough outcropping surface, and the
210 presence of FC), a more intensive sampling with distance to the FC were carried out
211 and this is detailed in the discussion section.
212 Just beneath the sedimentary coverage or on topographic highs, some outcrops
213 allowed sampling of the paleo-weathered layer. These are mostly non-cohesive
214 saprolite where some tectonic fractures traces are preserved thanks to oxide
215 precipitations (D, Figure 5a). The fractured layer under the saprolite could also be
216 sampled in the Northern Vosges area for granitic and granodiorite facies and Limagne
217 diorites. Sample numbers for the main basement lithologies in the three areas are
218 summarized in table 1.
219
220 After removing the weathered surfaces found around the samples, several
221 preparations were made: 1) thin sections for studying mineralogy and linking with
222 petrophysical measurements, 2) 25 mm diameter plugs (or equivalent volume pieces
223 when drilling was not possible) for apparent permeability measurements (k), water
224 porosity, skeletal and bulk density measurements, 3) 5-10 cm-wide blocks with
225 parallel faces for thermal conductivity (TC) and P-Wave velocity (Vp) measurement
226 in 3 directions, 4) 5 cm^3 pieces for Hg porosimetry determination, especially for the
227 non-cohesive samples.
228 In total, 155 blocks were measured in the Vp and 160 in the TC, 419 plugs for
229 water porosity and density, 112 for permeability and 105 for Hg porosity, with an
230 analysis of 249 thin sections for a total of 202 samples. The detailed analysis and
231 measurement methods are described below.
232

	Northern Vosges									
	Northern granites	Tardi-H granites	Fini-H granites	Granodiorites	Bruche unit	Rabodeau-Schirmeck unit	Diorites	BM volcanics	Southern schists	
Fresh	5	10	2	10	25	7	3	7	2	
Altered	1	7	2	3				1	3	
Fault Core		1	3		1	1		1		
WL fractured horizon	1	2		1						
WL saprolite		1	1							
	Southeastern FMC					Limagne Shoulders				
	Leucogranites	Calcalk - granites	LGU - gneiss	LGU - schists	UGU – gneiss	Granites	Visean metasediments	Diorites	Migmatites	
Fresh	10	3	1	1	3	4	3	2	1	
Altered	3	6	6	9		10	6	2	4	
Fault Core	5	1		3	1	6	2	6		

WL fissured horizon									
WL saprolite		2				3			

Table 1: Numbers of samples and qualitative structural positions for the main basement rock lithologies in the Weathered layer (WL) of the three areas.

3.1. Petrographic analysis

Several hydrothermal alteration stages should affect the WER basement due to the complex geological background (*Géraud et al 2010; Ledésert et al., 2010*). As a hydrothermal alteration is mostly recorded by transformation of the primary biotite, pyroxene, amphibole in chlorite or secondary clays and plagioclase, and K-feldspar in secondary clays (smectite, illite or kaolinite), these transformations have been semi-quantified in the thin-sections using optical microscope (*Pirajno, 2009)(*Figure 5*b)*, as well the microcrack densities and inter/intragranular porosity if observable.

3.2. Densities and porosity

The skeletal density ρ_s was measured five times with Helium porosimetry with the AccuPyc II 1340 of micrometrics® gas pycnometer. A triple weighing method was used to determine the bulk density and H_2O porosity. For this purpose, the plugs were saturated with distilled water following the RILEM norm (try n°I.1, 1978), allowing measurement of the saturated, w_{sat}, and hydrostatic, w_h, weights. The effective water porosity ϕ can thus be calculated following *equation 1*, with w_{dry}, the dry weight, V_{water} the saturated water volume and V_s the sample volume.

$$\phi_{H_2O} = \frac{V_{water}}{V_s} \times 100 = \frac{w_{sat} - w_{dry}}{w_{sat} - w_h} \times 100$$

Equation 1

Using the sample volume in equation 1, the bulk density ρ_b can be calculated as follows:

$$\rho_b = \frac{m_{dry}}{V_s}$$

Equation 2

Mercury porosimetry was used to determine the porosity value for the most altered samples that are noncohesive in water, but also to measure the pore throat diameter distribution. The experimental procedure is described in *Rosener and Géraud (2007).* Only the first injection step, allowing the description of the porosity distribution vs the pore threshold diameter is discussed in this study. A Visual Basic script was developed to detect the pore throat diameter where a significant porosity volume is injected. First, the incremental Hg injection volume is calculated for each pressure step. Then the maximum injected volume on a single step is detected. The pore size diameter associated with a significant porosity volume are then defined as where the incremental injection reached more than 40% of the maximum injected pressure at each pressure point. With empirical tests we notice that this procedure allows to separate one, two or three pore throat families in a single injection curve.

When the pore size distribution is too heterogenous, the threshold detection shows highly heterogenous detection that can be manually removed. From the widest to the thinnest pore throat detected on each pore throat family, the % of the whole porosity is calculated to compare the detected pore volume regarding the total porosity volume of the sample. Overall tested diameters range from $3.5x10^{2}$ to $5x10^{-3}$ µm.

3.3. Permeability

Apparent permeability *k* at room temperature and confining pressure between 15 and 20 bar has been measured on the plugs with a method described in *Rosener (2007)*. In the experiment, the permeability (k) is derived from the Darcy law with the mean apparent permeability k_a at different applied pressure P_h (*equation 3)*. This equation assumes a steady state flow and correction of the Klinkenberg effect (*Klinkenberg, 1941*). In the equation, R is the perfect gas constant, μ_g and M_g nitrogen viscosity and molar mass, L and S the sample length and section, and T the room temperature. This device allows the measurement of permeability from approximately 10^{-19} to 10^{-12} m^2. For low permeabilities outside of the measurement range, a $1x10^{-19}$ m^2 value is applied to plot a measured value in the paper.

$$k_a = \frac{RT}{M_g S} \frac{2Q\mu_g L}{{\rho_b}^2 - {\rho_h}^2}$$

Equation 3

3.4. Thermal conductivity and P-wave velocity

Both TC and Vp are functions of sample mineralogy (mineral thermal and elastic properties), of porosity volume and of structure type (fissures/pores), (*Belikov, 1967, Darot and Reuschlé, 2000*; *Surma and Géraud, 2003; Boulanouar et al., 2013*). The effect of petrographic and pore structures on samples of different alteration degrees will thus be compared with these two properties.

TC measurement was performed on a Thermal Conductivity Scanner from Lippmann & Rauen GbR (*Popov et al., 1999*), with the detailed procedure described in *Haffen et al. (2017).* To avoid effects of magmatic or metamorphic foliation, and also the effect of preferential microcrack direction, the samples have been scanned in three directions with measurement points every 1 mm. The thermal conductivity λ obtained ($W.m^{-1}.K^{-1}$) is the mean of three scans, with mean standard deviation on all samples of around 0.1 $W.m^{-1}.K^{-1}$.

The Vp measurements were performed in the same directions, with the pulse generator PunditLab from Proceeq®. Two piezoelectric transducers of 250 kHz or 54 kHz (depending on sample attenuation) were used to generate a sinusoidal pulse through the sample. The delay between wave emission and reception was measured and Vp calculated as a function of the sample width. The mean standard deviation of the overall samples in the 3 directions is around 0.2 $km.s^{-1}$.

Due to the negligible directional anisotropies of the two properties, only the mean values will be discussed in this paper.

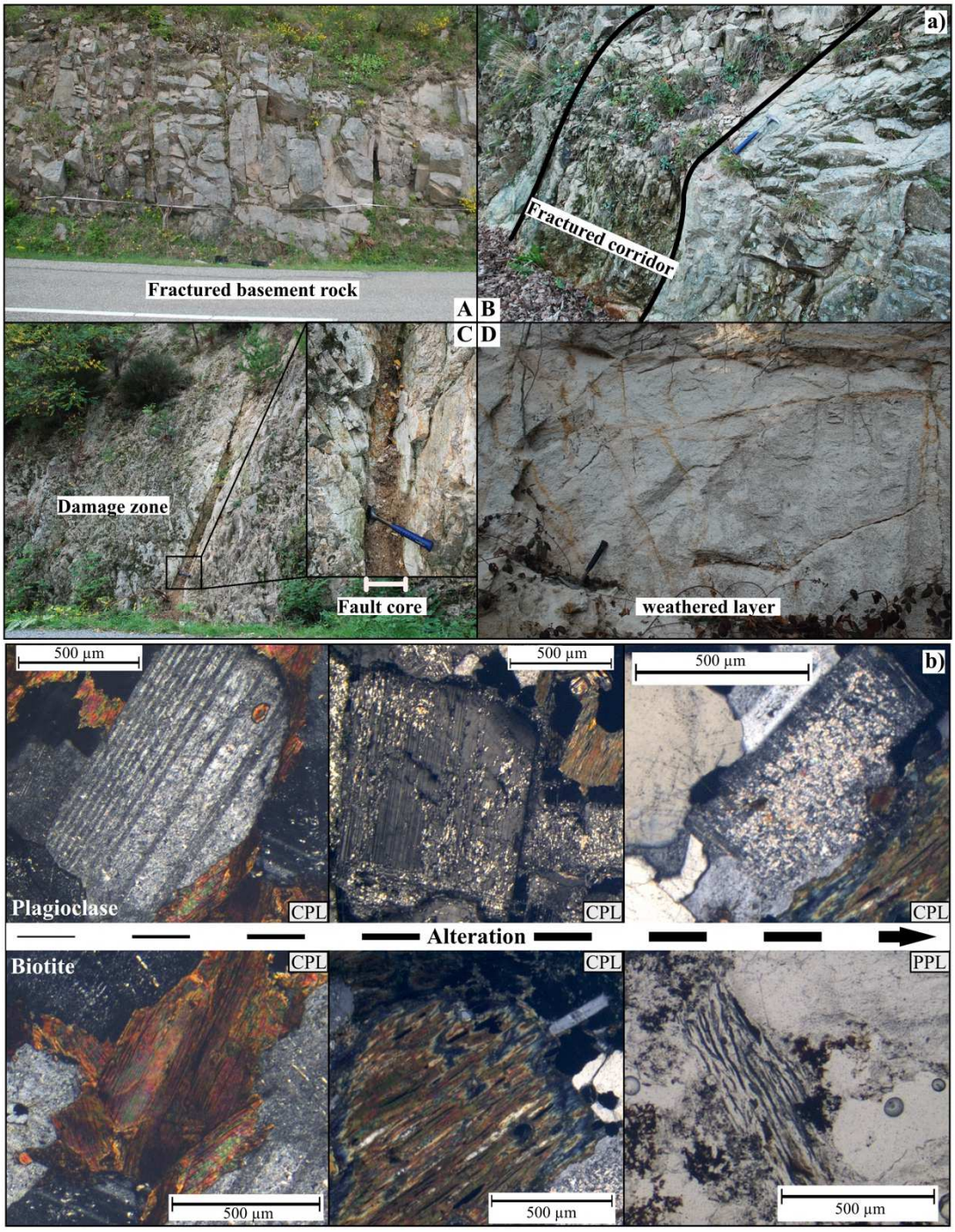

Figure 5: a) representative outcrop picture of fractured basement rocks (A) for fresh and altered samples, minor fault core and associated damage zone (B), fractured corridor (C) and a weathered layer in granite (D), b) examples of the mineral evolution with the alteration characterized in the thin sections study for plagioclases into illites and biotites in chlorites then clays, in Plane Polarized Light (PPL) or Cross Polarized Light (CPL).

4. Results

4.1. Mineralogic composition

From a petrographical point of view, three groups could be distinguished in terms of mineral alteration and microcracks density evolution in relation to their position in the fault zones. The sample locations will thereafter be designated as V for the Northern Vosges, L for the Limagne area and MC for the Eastern French Massif central. The first group was composed of the overall granites and granodiorites in the three areas studied. The second group was formed with the L-Visean volcano-sedimentary unit, the MC-gneiss and schists and the V-Bruche unit. Finally, the third group was composed by the L- & V-diorites and migmatites, V-metamorphosed samples ("Bande-Médiane", Rabodeau-Schirmeck unit and Southern schists). The petrographical variation with alteration in each group are discussed below and summarized in *the Appendices*.

4.1.1. Group I: granites and granodiorites

Despite variations in ferromagnesian minerals content and grain size, the overall granitic and granodioritic bodies have roughly the same mineralogy variability between the fault/weathered zones and unaltered samples. In weakly fractured areas, the samples were almost fresh. The biotite, muscovite or amphibole were slightly replaced by chlorite and oxides, and the plagioclase and K-feldspar were almost fresh. There were almost no open microcracks in the thin sections (*Appendix A)*, although many fluid inclusion alignments expressed the presence of a healed crack network.

In damaged zones, the fracture density was moderate. There, alteration led to partial replacement of the ferromagnesian, following the cleavage planes in the biotite and muscovite. The K-feldspar and plagioclase are also partially replaced by clays, with a transformation that is sometimes guided by a few microcracks, but that is not the general case. These transformations are more intense in the highly damaged rocks in fracture clusters, leading to a complete dissolution of the primary minerals even if the primary grain boundaries are preserved (*Appendix A*).

All fault cores sampled in the granite and granodiorite bodies were incohesive breccias or cataclasites partly cemented with secondary clays. In thin sections, the K-feldspar and plagioclase grains were only detectable with their old grain boundary traces, but they were totally replaced by clays. These clays filled the micro-cracks network, accompanied by oxides, but macro-porosity can also be observed (*Appendix A*). In these samples, the ferro-magnesian minerals were totally dissolved and identifiable with the old cleavage planes followed by clay and oxide precipitation.

Finally, in the saprolite thin sections, the K-feldspar and plagioclase grains were almost fresh, and the ferro-magnesian minerals only showed weak transformation namely with iron oxides that precipitate in the surrounding micro-cracks (*Appendix A*). In contrary to the DZ samples, the open micro-crack density was very high in the quartz but also in the K-feldspar and plagioclases and seemed to be spatially linked with the ferromagnesian minerals.

4.1.2. Group II: main metamorphic units

In a first approximation, the mineral composition of the main metamorphic units could be described with two end-members: 1) the V-Bruche and L-Visean samples as well as the MC-Schists are fine-grained with quartz - feldspar and biotite - muscovite - chlorite bends in various proportions, with massive facies (graywackes, pelites) or with a well-marked schistosity. Microcracks are generally present in all samples, including the protolith. In the schists, the microcracks are concentrated in the

quartz bends and veins or open the existing schistosity. 2) Some samples derived from conglomerates or volcanic facies in the V-Bruche and L-Visean, as well as the MC-gneiss are composed mainly of coarse-grained quartz, feldspar, plagioclase and ferromagnesian phenocrystals in a more or less plentiful fine-grained matrix. In L- and MC-, the quartz grains were often subjected to high temperature recrystallization associated to the regional metamorphism.

In the fractured areas and damaged zones, the mineral alteration was similar to that of group 1 samples (*Appendix B*): an increase of the clay content in the plagioclase and K-feldspar phenocrystals or bends and a partial to total chloritization of the ferromagnesian minerals. In addition to this chemical alteration, the density of microcracks increased in the fine-grained facies, particularly crosscutting the quartz bends in some cases or opening the schistosity planes in others. This network was partly filled with quartz or iron oxides and to a lesser extent with carbonates.

All FC samples taken in this group showed a high density of microcracks, with a variable mineral alteration (*Appendix B*). In graywackes of the V-Bruche unit, the FC was fully argilized and non-cohesive. In the gneiss, the quartz bends supported the argilized matrix in cohesive breccias. In the L-Visean unit, the FC samples show a weak mineral alteration but a high density of microcracks filled with quartz, clays and oxides.

4.1.3. Group III: massive rocks

This group is distinguished by a general observation that there are very few mineral alterations that are not directly correlated with the fracture intensity in the damaged zones. It is mostly an increase of the microcrack density that characterizes the evolution in the fault zones (*Appendix C*). In L- & V-diorites and L-Migmatites, the alteration process led mainly to weak argilitization of the feldspars and alteration of the ferromagnesian minerals, with a lower intensity than for groups I & II (*Appendix C)*. The microcrack network was partly filled with various minerals, such as quartz, chlorites, clays and carbonates, depending upon their location.

For the V-Southern Schists, the thermal metamorphism associated to the plutonic intrusion led to an overprinted schistosity. Unlike the schists in group II, these were not affected by mineral alteration. FC with breccias and altered minerals were only found in L-diorites, while in the other facies there were mostly fractured corridors. In the FC studied, many secondary quartz and carbonate fracture in-fillings were preserved (*Appendix C*). At the few outcrops where the contact between the basement rocks and the post-hercynian sediments could be observed, there was no significant weathered layer.

4.2. Petrophysical properties

The petrophysical measurements are presented in this section in light of the three groups distinguished in the petrographic analysis. For each group, the skeletal and bulk densities will be presented in relation to the porosity evolution between the fresh, altered and fractured clusters and FC samples. The link between the porosity and pore throat diameter, matrix permeability (k), and TC and Vp property evolutions will be presented later.

4.2.1. Group 1: granites and granodiorites

The H_2O porosity of the overall cohesive granites and granodiorites samples ranged from 0 to 16.5 %.

The skeletal density ranged between 2.58 and 2.80 $g.cm^{-3}$ with a mean value of around 2.67 $g.cm^{-3}$ for all samples and an almost flat trend, i.e. there is no variation with the porosity (Figure 6*a)*. Abnormal High skeletal density values are only obtained for some samples in a fault zone in the L-Saint Dier granites, where the mineral alteration is associated to pyrite mineralization. V-granodiorites have slightly higher densities than the full sample set, due to the difference in content of ferromagnesian minerals and plagioclase/K-feldspar proportion.

The bulk density of the overall samples demonstrated linear decreases with the porosity following the equation shown in Figure 6*b*. These trends on skeletal and bulk densities highlighted the evolution between fresh and altered samples and pointed out that: 1) the primary mineral alteration did not influence the whole rock density as its increase did not change the skeletal density, and 2) there is no development of unconnected porosity. Roughly, the fresh samples porosities were between 0 and 3 %, and the porosity is increased with the alteration until most altered samples in the DZ at ≈ 11 %, the saprolite and FC samples being between 6 and 16.5 %. The skeletal density determined from the equation is 2.67 $g.cm^{-3}$, similar to the value obtained from the nitrogen pycnometer.

On the Hg-porosity, the samples with porosity ≤ 8.3 % were also mainly fresh and altered samples. They showed preferential pore throat diameters between approximately 5 and 0.005 µm, with 36 to 89 % of the total Hg-porosity (Figure 7). These diameters varied slightly between the samples but did not show a significant increase with the total porosity. The porosity variation followed the mineral alteration development observed in the thin sections. For the samples with porosity > 8.3 %, a larger pore throat diameter family developed in addition to the first one, between 10 and 285 µm, (Figure 7). These samples were all FC and saprolite, and they showed significant microcrack densities in thin sections that could be linked to their second pore throats. Only one is a saprolite sample with less than 8.3 % porosity, but both characteristic pore families are also observed for this sample. We could notice that the maximum porosity for non-cohesive samples could reach 52 % for FC and 33 % for saprolite.

The matrix permeability showed a rapid increase between fresh (with porosity < 3 %) and the altered samples. It ranged between $1x10^{-19}$ and $4x10^{-16}$ m^2 for the fresh samples, and the altered samples ranged between $2x10^{-18}$ and $2x10^{-13}$ m^2 (Figure 6*c*). However, this increase was not linear, and it showed a high variability for samples with porosities ranging between 2 and 8 %. The permeability was only measured for two samples with a porosity higher than 8 % due to the incohesiveness of most FC and saprolite samples. One was at $5.7x10^{-18}$ m^2 and the other at $8.6x10^{-15}$ m^2 that suggests a high variability of this property for FC and saprolites.

Also, the alteration increase showed a linear evolution of densities with porosity, the TC and Vp almost followed this trend (Figure 6*d*). Thus, with the increase in porosity, the thermal conductivity and the P-wave velocities decreased linearly even if there was some variability due to rock facies variation, like grain size or ferromagnesian mineral content. From fresh to highly altered samples in the damaged zones, the TC decreases from ≈ 3.0 to 1.7 $W.m^{-1}.K^{-1}$ and the Vp falls from ≈ 5.4 to 1.9 $km.s^{-1}$. Saprolite samples show even lesser values, with a minimum TC at 0.7 $W.m^{-1}.K^{-1}$, and Vp until 1.7 $km.s^{-1}$ and even less for few samples where attenuation due to porosity was too important to allow determination of a value.

These observations were confirmed for most samples when TC and Vp were plotted against porosity (Figure 6*e & f*). For TC, a linear relationship with porosity was observed, even if this was very scattered (R^2= 0.18). The only exception was the L–Saint Dier granites that were mineralized with Pyrite. For Vp, there was also a linear relationship despite a group of samples with abnormally low Vp values regarding the porosity. The group is composed of fractured samples from altered facies and fissured layers.

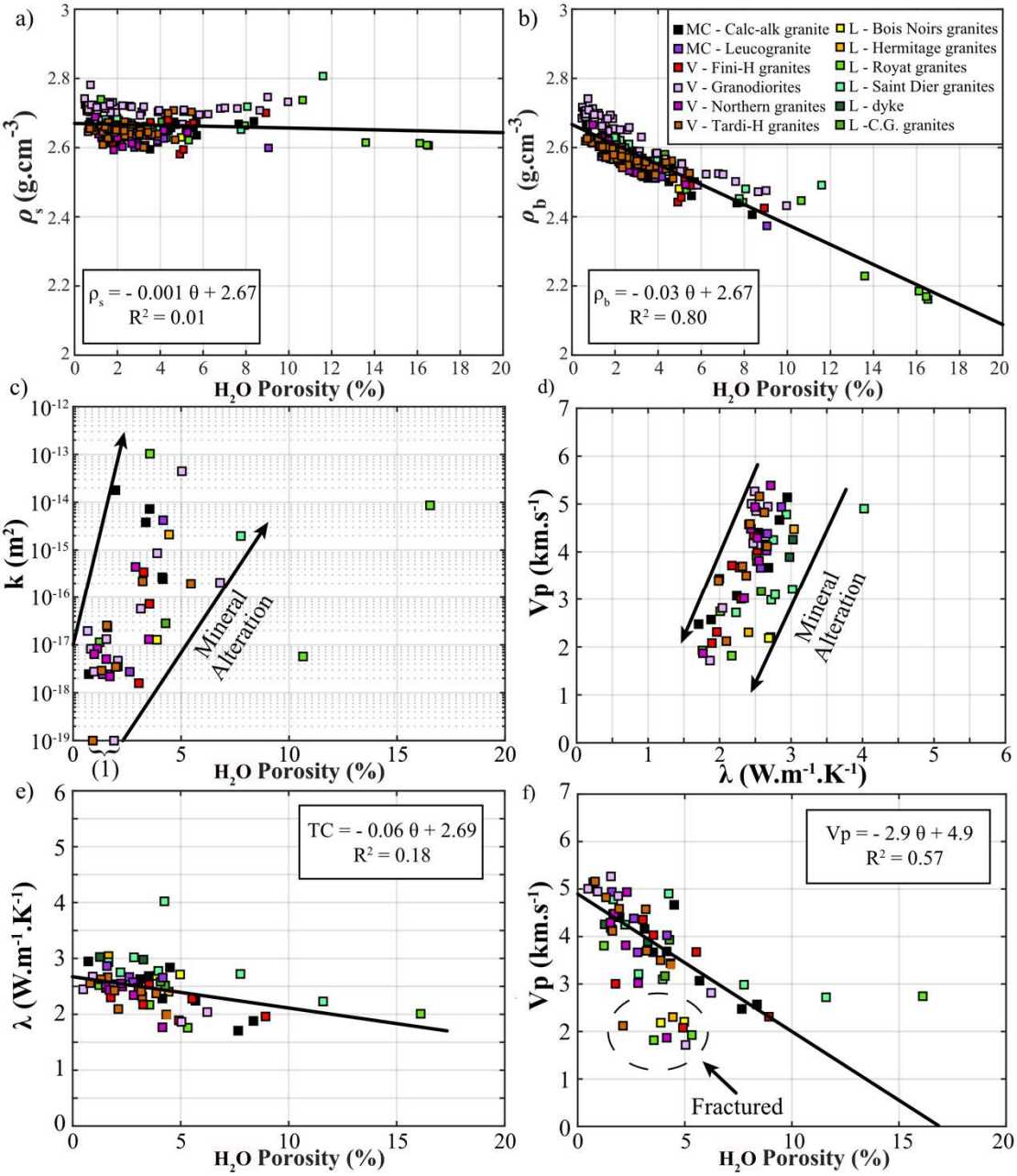

Figure 6: Petrophysical properties of group I samples: a) skeletal density, b) bulk density and c) matrix permeability vs porosity, d) Vp vs TC, e) Vp and f) TC vs porosity. For the two samples with (1) in figure 6c the permeability is too low for our measurement system.

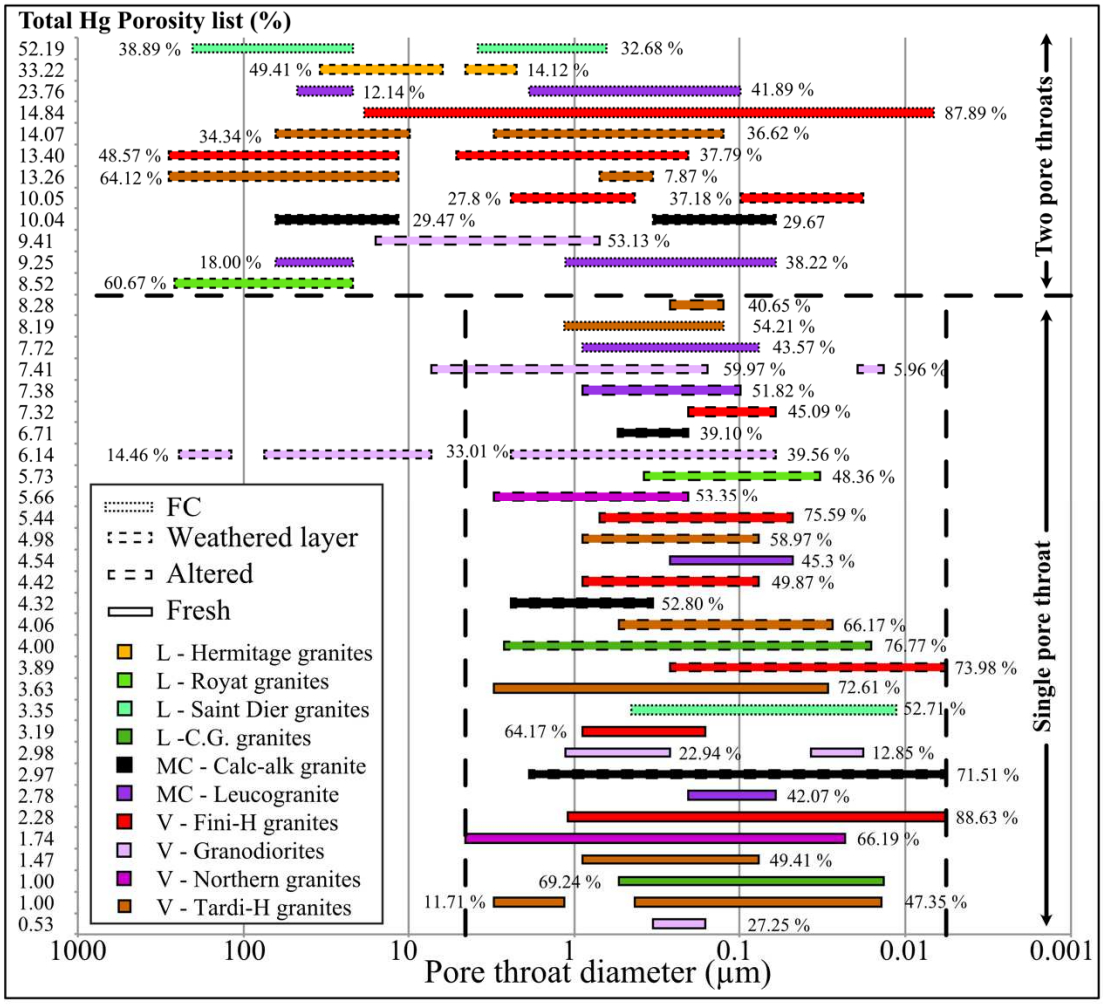

Figure 7: Detected pore throat diameter on Hg porosity of group I samples classified by increasing total porosity. Rates shown on the bars are the percentage of the total Hg porosity available through throat families. Dashed lines show domains with mainly one and two pore throats families.

4.2.2. Group II: main metamorphic units

H_2O porosity of the main metamorphic units of the three areas ranged between 0 and 18.8 %. The skeletal density showed a slight increase, mainly due to the facies variability that scattered the density values in particular for samples with porosity above 5 % (Figure 8a).

As for group I, the porosity shows a linear relationship with the bulk density, slightly sparser due to the facies variability, notably in the V-Bruche unit (Figure 8b). The bulk density of the fresh samples was 2.67 $g.cm^{-3}$ and this decreased less with porosity. However, the porosity variation was not correlated to the alteration degree between the protolith and DZ samples. In the V-Bruche unit and MC-LGU-Schists for instance, fresh samples had a porosity between 0 and 10 % as the altered ones varied between 1 and 13 %, depending on the microcracks and opened-schistosity plane densities. In these anisotropic facies, the secondary minerals linked to the alteration could also reduce porosity.

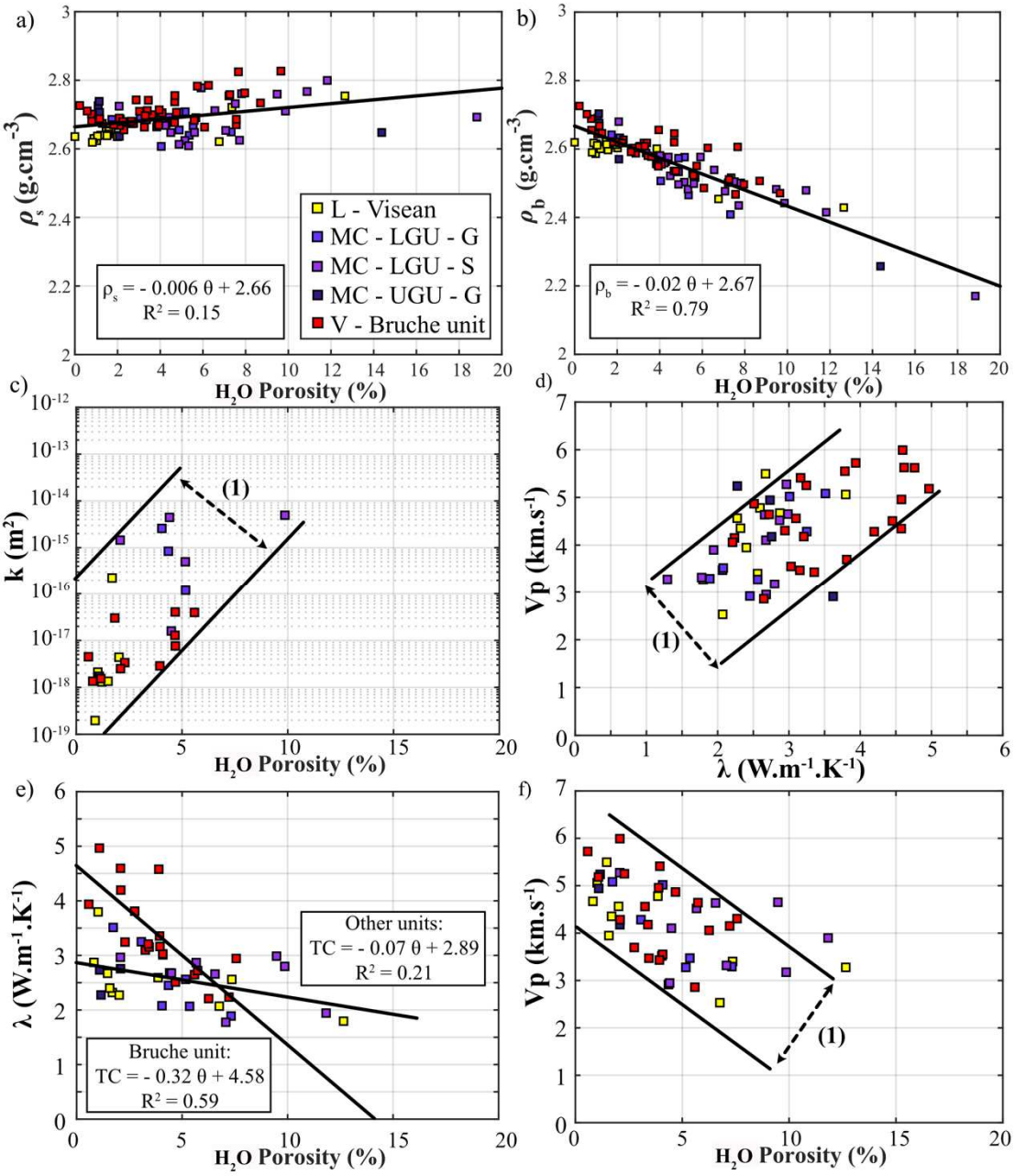

Figure 8: Petrophysical properties of group II samples: a) skeletal density, b) bulk density and c) matrix permeability vs porosity,d) Vp vs TC, e) Vp and f) TC vs porosity, (1) intervals between the double black lines show the variation ranges due to the microcrack and opened-schistosity planes density.

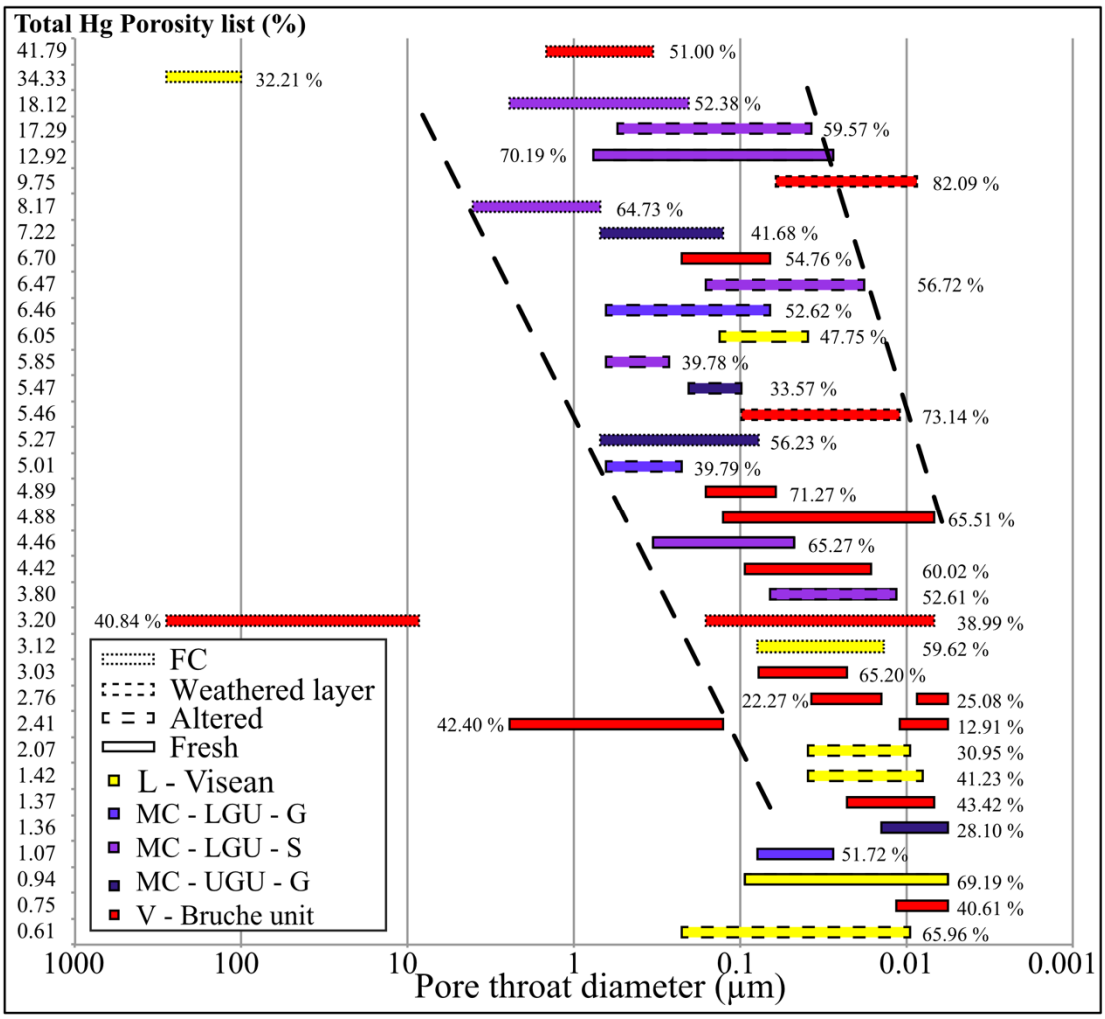

Figure 9: Detected pore throat diameter on Hg porosity of group II samples classified by increasing total porosity. Rates on the bars are the percentages of total porosity available through throat families. Dashed lines show the global pore throat enlargement.

Except for three samples, the Hg-porosity showed a single pore throat diameter as for the group I (Figure 9), but: 1) with smaller diameters and a thinner variation range (0.005 to 0.011 µm for the lowest porosities) suggesting a more organized pore volume; 2) this pore throat family increased and enlarged slightly with the total porosity until 0.3 - 1.1 µm. No second wider pore throats were observable for the most porous FC samples, suggesting that the microcrack networks do not create distinct pore throats. The three exceptions to this pattern were a Bruche unit conglomeratic facies with wide interclast pores not present in the other facies (porosity = 2.41 %), and brecciated FC samples (porosity = 3.20 and 34.33 %) with open microcracks in contrast to the other FC samples of this group, which mainly had mineral alteration. It can be seen that the FC samples of this group can reach 42 % porosity.

For all cohesive samples, the matrix permeability showed a high variability that was independent of the porosity values (Figure 8c). Depending on the opened-schistosity planes and the microcrack densities, the permeability varied between 2.0×10^{-19} and 5×10^{-15} m^2 for samples with porosities ranging from 0 to 6 %. The most permeable facies were therefore the MC–LGU and UGU units where the schistosity is

in general more expressed than in the V–Bruche and L–Visean units. Only one FC sample at 5.10^{-15} m^2 permeability and 9.6 % porosity could be measured.

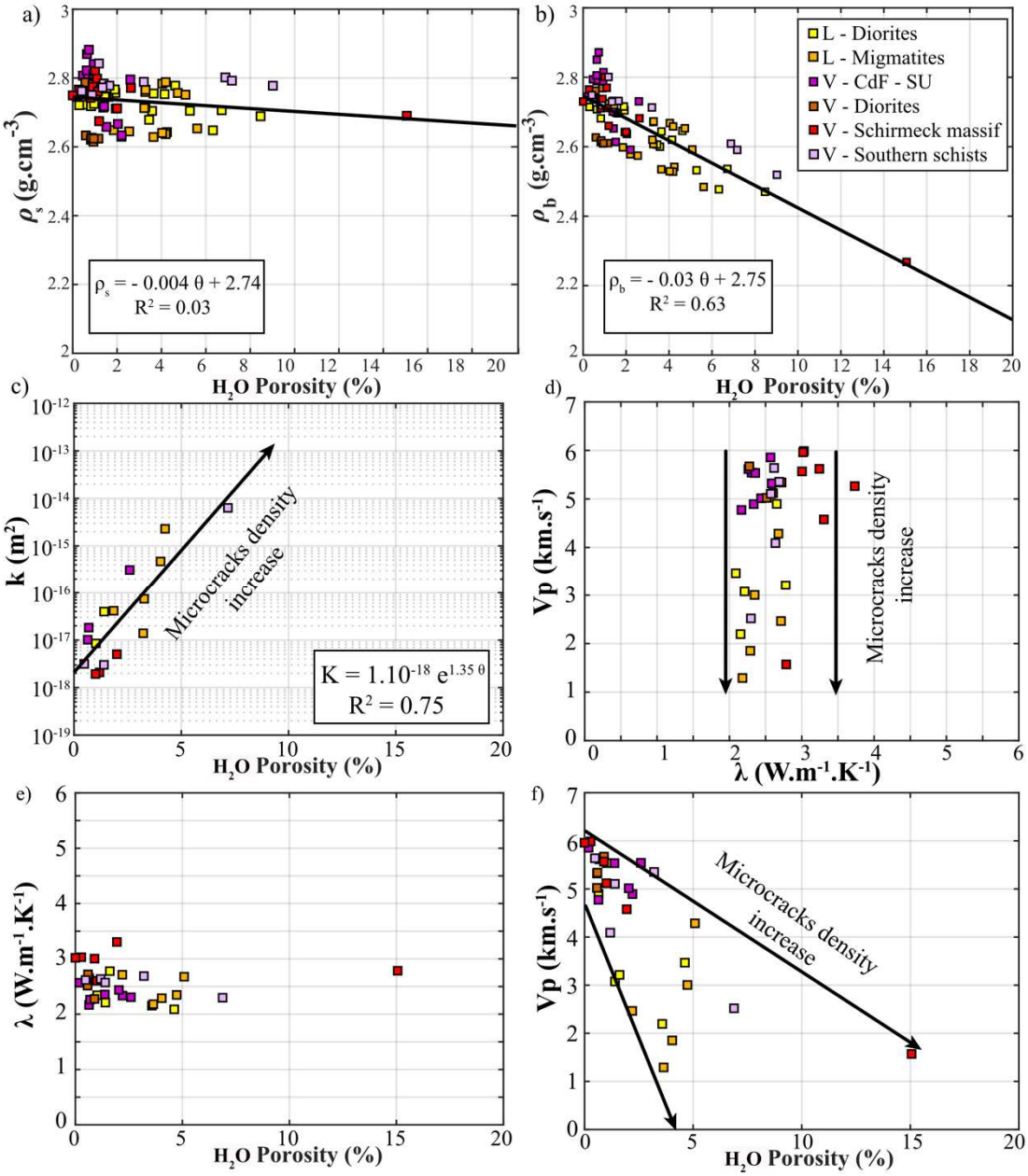

Figure 10: Petrophysical properties of group III samples: a) skeletal density, b) bulk density and c) matrix permeability vs porosity, d) Vp vs TC, e) Vp and f) TC vs porosity.

The TC and Vp expressed the high variability of rock facies even if there is a general proportionality between the two properties (Figure 8d). Furthermore, no specific relation with the petrographic variation between fresh and DZ samples was identified. However, two subgroups could be identified: some samples of MC-Schists and the V-Bruche unit with mainly quartz and K-feldspar content had around 1-1.5 $W.m^{-1}.K^{-1}$ more TC than other facies for the same Vp. This highlighted the difference in quartz content but also the fact that microcrack densities were generally higher for these samples. TC against H_2O porosity reflected the scattering of the rock facies, the

V-Bruche unit showing a more intense decrease with porosity than other samples (Figure 8e). The Vp measured against H_2O porosity is also scattered, but the general trend of a decrease with porosity was valid for all facies.

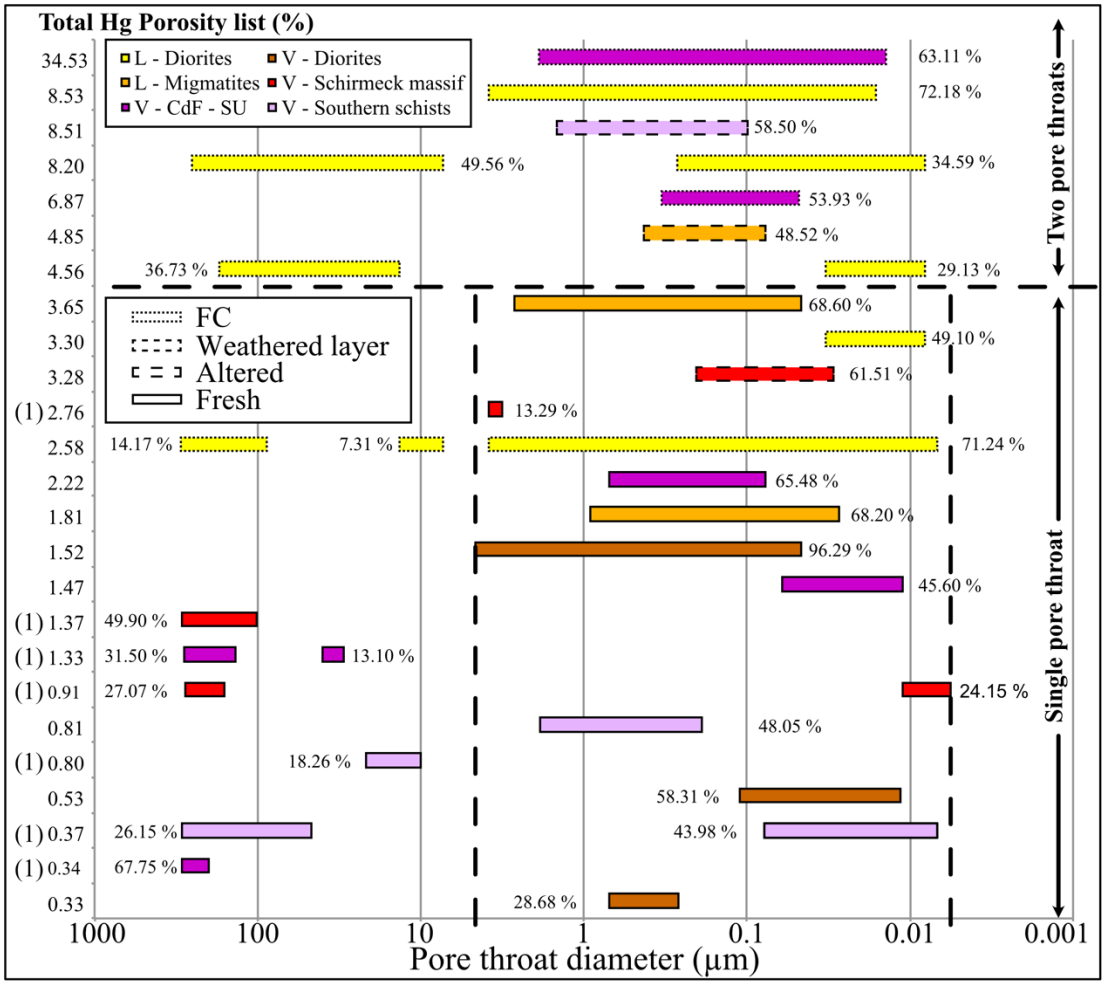

Figure 11: Detected pore throat diameter on Hg porosity of group III samples classified by increasing total porosity. Rates on the bars are the percentage of total porosity available through throat families. Dashed lines show domains with mainly one and two pore throats families, (1) are samples were the pore throat were nott properly detected (homogenous pore size distribution).

4.2.3. Group III: massive rocks

The H_2O porosity of the massive rocks ranged between 0 and 15.1 %, but many of them are under 2 % and only a few exceed 5 % (Figure 10a). Those between 3 and 6 % are the altered facies of the L–Migmatites and Diorites, and those > 5 % are the FC samples in the L-Visean unit and an altered V-southern schist. The skeletal density varied between 2.6 and 2.8 $g.cm^{-3}$ and highlighted the petrographic variability, without a clear correlation with the porosity, leading to an almost constant linear trend (Figure 10b). The linear relationship between the bulk density and porosity remained, with a density of 2.75 $g.cm^{-3}$ at zero porosity, i.e. higher than groups I & II, and almost equal to the mean skeletal density.

The Hg porosimetry shows very scattered pore throat diameters (Figure 11). For most samples of Hg porosity < 3 %, the automatic pore throat detection did not reveal significant injection peaks, only the first injection steps or changes between low- and high-pressure phases were detected. For these cases, the Hg was almost homogenously distributed over all pore throats. However, for the samples where pore throats were detected, the porosity distribution could be considered as similar to that of group I, with a threshold of 4.5 % instead of 8.3 %: 1) a thin pore throat family between 0.01 and 2 µm for samples < 4.5 %, mainly composed of fresh samples with a few altered ones and 2) a larger pore throat family that appears at porosities above 4.5 %, with mainly the FC samples (Figure 11). It can also be noticed that even altered and FC samples never reach more than 8.5 % porosity, except for CdF 38 that is a centimetric scale mineralized filling in fractures of the V-CdF southern units.

In contrast to the facies variability highlighted by the densities, the permeability evolution fitted very well with the porosity increase, describing an exponential trend with a good correlation factor (Figure 10c). Thus, the less porous samples have matrix permeabilities between $3x10^{-19}$ and $5x10^{-16}$ m^2 and these values increase until $6x10^{-15}$ m^2 for the most porous ones. As most of the samples were not or weakly subjected to mineral alteration, it would seem that only the microcrack networks influence porosity and permeability, while we have shown that in the other groups the alteration vs microcracking creates a more scattered behavior for this property.

This is also shown by the Vp and TC diagram, where there is no real diminution of TC with Vp. Samples gave TC values of between 2.1 and 3.7 $W.m^{-1}.K^{-1}$ with the highest values for the V-Schirmeck volcanics (Figure 10d). Independently, the Vp showed large variations, with values between 1.3 and 6.0 $km.s^{-1}$, with roughly two subgroups: the V-samples with Vp above 4.5 $km.s^{-1}$ and the L - Migmatites and Diorites with Vp under 4.5 $km.s^{-1}$. This high variability could be explained by microcrack densities that is significantly higher for the second subgroup. Thus, just as the TC reflects the mineral composition variability, the change in Vp can be attributed to sample microcracking in the fault zone (FZ). These trends are confirmed as TC does not show a significant decrease with porosity (Figure 10e) but it is the case for Vp, even if the trend is scattered due to rock facies variability (Figure 10f).

5. Discussion

5.1. Basement rock property evolutions in fault zones and weathered layers

Our petrophysical measurements are generally in agreement with published data concerning basement rock facies for outcrop or core samples, even if the ranges of these properties are very large (*see for example Čermák and Rybach, (1982) for TC or Morrow (2000) and Stober & Bucher (2007) for k*). The linear relationship between TC and Vp, densities or porosities are also highlighted in other areas (*e.g. Mielke et al., 2017; Weinert et al., 2020*).

The high variability of rock facies collected in the three areas of interest gives a first order characterization of the evolution of matrix properties in basement rocks and particularly in fault zones and some parts of the weathered layer. Although there is a lack of some specific facies like the ultrabasic rocks that locally outcrop in the Moldanubian domain, or some facies of the heterogenous metamorphic units in the Vosges. From the overall rock facies variability, three groups can be distinguished with a different evolution between the protolith, DZ, FC and saprolite samples that are

highlighted by the petrophysical measurements. However, the general poor outcrop quality does not allow systematic sampling of fresh, fractured DZ, and FC on the same outcrop for all rock facies. The few locations where FC could be sampled offered the opportunity to discuss more precisely the petrophysical variations with the position in the DZ (Figure 12).

For all three groups, the FC samples are in general gouges or breccias with significantly higher porosity than the DZ and protolith samples (Figure 12). This suggests that the FC could act as a conduit for fluid flow if secondary clays will not plug the pores and reduce permeability (*Bense et al., 2013*). For the DZ, the general models for basement rocks suggest conduit behavior due to fracturing and matrix alteration linked to fluid flows (*Faulkner et al., 2010; Bense et al., 2013*). In many cases, the enhancement of fracturing and alteration is considered as a progressive increase from the protolith to the FC (*Beach et al., 1999; Cello et al., 2001; De Joussineau et al., 2007; Mitchell & Faulkner, 2009*). For the alteration and linked matrix porosity and permeability development, our data are not in agreement with these simplified models.

In fact, the samples taken at the immediate border of the FC are actually the most porous of the DZ, but for the others there is no general increase in porosity (Figure 12). For the V - granites, and in the V-Bruche unit, the samples in the vicinity of the FC are even less porous than in the far-field DZ (a, b & d, Figure 12). Thus, only the FC and their immediate border can be considered to have good reservoir properties for the matrix. In the far-field DZ, the matrix properties are more randomly distributed, depending on the presence of individual fractures or of clusters of these that allow fluid flow and the subsequent alteration and reservoir property enhancement (Figure 13).

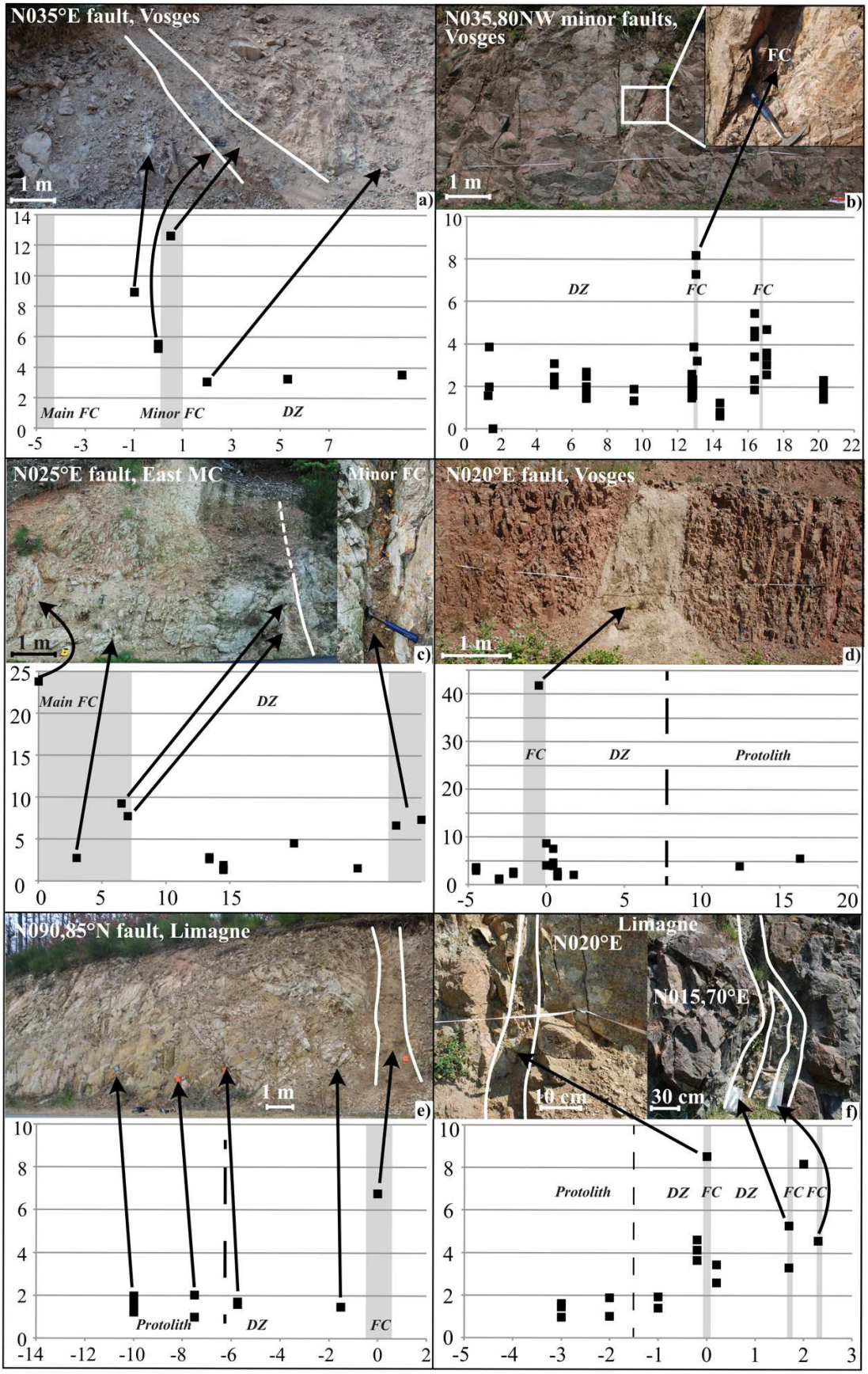

Figure 12 : Specific fault zones and porosity evolution through FC and DZ for a) & b) V - granites, c) MC - granite, d) V-Bruche unit graywackes, e) L-Visean unit and f) L-Diorites. All graphs are in porosity (%) vs distance (m).

Thus, the DZ in the granites and granodiorites (group I) expose local variations of the porosity linked to the mineral alteration process. This is accompanied by the development of high porosity and permeability in some parts and preserve almost fresh rocks in others, depending on the hydrothermal fluid flow (Figure 13a). In the DZ, this alteration creates a connected porosity (until ≈ 8 %) with fine pore throats (0.5 - 0.02 µm) that engender a linear diminution of the bulk density, of TC and Vp, and an increase of permeability from 10^{-18} to 10^{-13} m^2. In the FC and highly fractured clusters, the microcrack network, combined to alteration, creates a larger pore throat family (10 - 285 µm) and an increase of porosity that can reach 52 %. Unfortunately, the permeability of these last samples could not be measured.

In the metamorphic rocks of the group II, the porosity and permeability in the DZ is more distributed, and depend on the mineral alteration and on the microcracks density, in particular when the schistosity planes are well-oriented for being reactivated as fractures (Figure 13b)(*Bertrand et al., 2018*). This contrasted variation is reflected in the petrophysical measurements where fresh samples are not less porous. Thus, samples with only mineral alterations are more subject to porosity reduction whereas fracturing plus alteration led to porosity increases. In the same manner, the FC samples are subjected to alteration and fracturing but with an increased intensity, leading to higher porosities, of up to 42 %. The skeletal density, the permeability, the Vp and TC measurements are sparse according to this petrographic variability, as the Hg porosity shows not more than an increase of the mean pore throat diameter (0.005 - 0.011 to 0.3 - 1.1 µm) with the increase of total porosity.

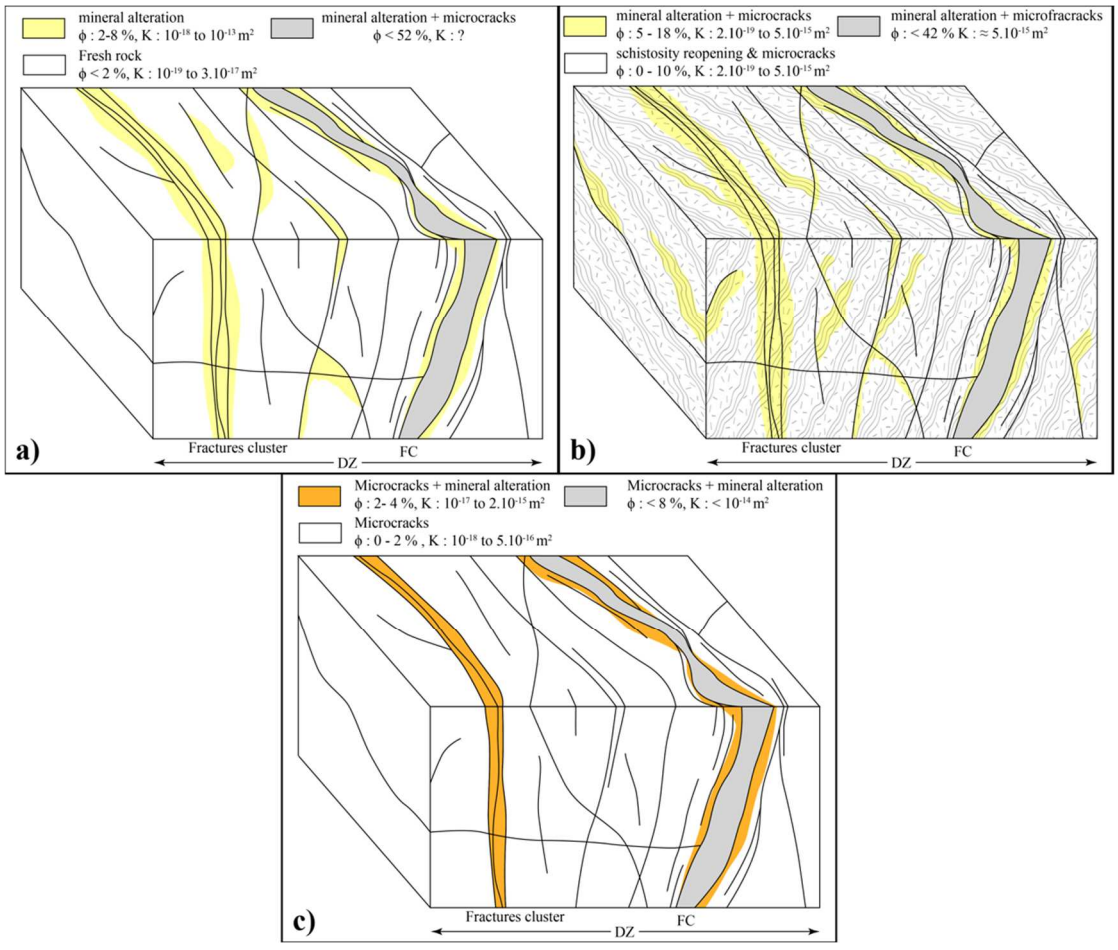

691 *Figure 13: Conceptual model of fault zones at the outcrop with hydrothermal*
692 *alteration and linked porosity for a) the granites and granodiorites, b) the main*
693 *metamorphic units and c) the massive rocks.*

694 Finally, for the more massive high temperature or thermally metamorphosed
695 diorites and metamorphosed volcanics of group III, no distinct mineral alteration is
696 recognized in the protolith and DZ samples (Figure 13c). They are only subjected to
697 microcrack density increase that led to weak porosity increases, and in consequence a
698 decrease of Vp as the TC is almost constant. These microcracks develop a porous
699 network with distributed pore throats and a linear increase of the matrix permeability
700 from 10^{-18} to 10^{-14} m^2. The mineral alteration process is only concentrated in the FC
701 and some local fracture clusters. Despite this mineral transformation, the total
702 porosity of the FC is significantly lower than for the two other groups, with a
703 maximum value measured as around 8.5 %.
704
705 The weathered layers were unfortunately only sampled in the granitic bodies
706 where distinct non-cohesive saprolites facies were recognized. As it could be due to
707 the outcropping and paleo-topographic conditions in the three areas, it suggests that
708 the non-granitic basement rocks are less favorable for the development of such layers,
709 or at least that the weathering phenomenon is less efficient for these facies (*Dewandel*
710 *et al., 2006; Velde et Meunier, 2008*). In the granites, these samples are clearly
711 different from the others, with a high-density microcrack network, spatially linked to
712 the ferromagnesian minerals, while the other primary minerals do not show significant
713 alterations. They show high values of Hg porosity of up to 33 %.
714
715 5.2. Comparison of the models with borehole data
716
717 The direct comparison of property values with existing data from deep
718 reservoirs is not simple because there is a shift between the petrophysical properties
719 measured on dried outcrop sample and cores sampled in depth (i.e. confined and
720 saturated rocks) (*Kranz et al., 1979; Morrow et al., 1994, Morrow, 2000*) or with
721 geophysical well-logs (*Esteban et al., 2015).* However, the general models presented
722 in this paper can be qualitatively compared with FZ architecture in borehole data,
723 especially in the URG where the Soultz-sous-Forêts and Rittershoffen geothermal
724 boreholes aimed to use fluid flows in fault zones in granites and immediate
725 sedimentary cover. The two geothermal projects at Insheim and Landau also target
726 fault zones in granites but there is no detailed petrophysical and petrographical
727 variation published yet (*Vidal et Genter, 2018*). For the other lithologies, sadly there
728 is a lack of in-situ petrophysical data, even if some studies on hydraulic data suggest
729 that high temperature metamorphic rocks are less permeable than granite type
730 basements (*Stober and Bucher, 2007*).
731 At Soultz-sous-Forêts, the fully cored EPS1 highlighted different rock facies
732 due to fracturing and hydrothermal alteration of the rock mass (*Ledésert et al., 2010*).
733 The overall range of property variations in the drilled granites with TC values of
734 between 2.3 and 4.3 $W.m^{-1}.K^{-1}$, k between 10^{-20} and 10^{-14} m^2 (*Hettkamp et al., 1999*)
735 and porosity between 0.13 and 25.55 % (*Géraud et al., 2010*) is in agreement with the
736 ranges of the group I granites in this study. From fresh to altered facies there is a
737 similar porosity evolution. Only the most porous samples have a different trend: In
738 Soultz-sous-Forêts they are not permeable due to clay neoformation (10^{-18} m^{-2} for 10
739 % porosity) (*Géraud et al., 2010*) and pore throat diameters are between 0.3 and 0.006

μm which is significantly smaller than group I samples (*Rosener & Géraud, 2007*). These porous facies in the well are located randomly in the FZ and create local fluid conduits that are not correlated to the main FC distance. In Rittershoffen wells, the permeable zones are also located in a few fractured clusters linked to local alteration facies in the DZ (*Glaas et al., 2018*). However, these facies are partly plugged by secondary precipitation of calcite, illite and chlorite (*Vidal et al., 2017*). Unfortunately, in Rittershoffen no cores are available for the precise quantification of petrophysical property evolution.

The petrophysical properties evolution from the Soultz-sous-Forêts wells and the repartition of the porous (altered) facies in the FZ from the Rittershoffen wells are therefore in agreement with our proposed model for group I. It is likely that the paleofluid uses preferential flow conduits which interact with the rock mass and locally enhance reservoir properties with a spatial repartition that is not corelated to the FC distance. Also, as the permeability of the most porous samples of the study could not be measured, the same effect on permeability reduction despite the porosity increase can be expected.

For the weathered layers, the two well-sites do not show evidence of a saprolite layer that was preserved during the basement burial, but both have typical iron oxydes filled horizontal fractures and mineral alteration belonging to the deepest part of a typical weathered layer development (“*fissured layer”, Dewandel et al., 2006).* In Rittershoffen wells*,* no significant permeability was detected during injection operation in this layer (*Vidal et al., 2016*), but analyzed core samples from Soultz-sous-Forêts show matrix porosity between 5.6 and 7.0 % and permeability around 1.10^{-18} m^2 (*Géraud et al., 2010*). Our measurements on saprolite layer samples that schematically lie above the fissured layer shows porosity significantly higher to these values, until 33 % for group I granites. It could indicate that the weathered layer of the basement should be a significant permeable layer for geothermal purpose in other parts of the basins where it is more preserved than in the actual drilled wells in the WER.

Some authors claim that a direct comparison between outcrop analogs is hazardous because there is a difference in the fracture network and porosity properties between the outcropping shoulders and the URG in depth rocks (*Bauer et al., 2017; Kushnir et al., 2018).* Extensive sampling in the three areas studied showed that the lithologies have a similar response to the hydrothermal alteration and should therefore be applied for predictive modelling in fluid flows in basement rocks for future drilling programs in the WER grabens. Our synthetic models can for example supply dual-porosity models to give a first level of rate and pressure of flow modelling in targeted fault zones before the drilling and injection operation. Some papers state how the TC and Vp react to confining pressure, fluid saturation or temperature (*e.g. Morrow, 2000; Mielke et al., 2017*). Combining such studies with the relationships we showed between the different properties for each petrophysical group will allow progress in the development of these models.

Conclusions

With the three areas of interest, our study offers a first order overview of the reservoir properties of fault zones in the basement rocks of the WER grabens. As these structures are the targets of several drilling programs, namely with high temperature geothermal prospects, estimations of these properties are essential for pre-drilling resource evaluations. The weathered layer at the top of the basement rock

790 can also be a significant reservoir, therefore samples of this layer are also included to
791 the dataset.
792 The extensive data collection in the three locations studied shows three groups
793 with similar petrophysical property evolution in the FZ despite the high initial
794 petrographic variability. Thus, the granite and granodiorite facies (group I) show
795 mainly mineral alteration in the DZ, with only substantial microcracks in the FC and
796 local fracture corridors. In contrast, the diorites, migmatites and thermally
797 metamorphosed facies (group III) are subjected to microcracking in the DZ with only
798 mineral alteration in the FC. The fault zones in the other metamorphic units (group II)
799 expose an intermediary process between the two other groups, with a combination of
800 mineral alteration and microcracking, depending on the primary mineral composition
801 and orientation of the potential existing schistosity. These led to different
802 relationships between porosity and permeability properties and associated skeletal
803 density, TC and Vp evolution, with only a simple exponential increase of permeability
804 with porosity for the fractured group III samples.
805 The weathered layers are only found developed in the granites and
806 granodiorites, suggesting that the other rock facies are less susceptible to develop or
807 preserve such layers in the Hercynian domains. For granite saprolites, microcracking
808 linked to the ferromagnesian mineral seems to be the main process of weathering,
809 leading to non-cohesive and highly porous facies.
810 The basement rocks, especially granites, are often considered as poor reservoir
811 quality for the matrix (*Nelson, 2001; Gutmanis et al., 2015; Kushnir et al., 2018*) and
812 main flows concentrated in few well-connected fractures (*Vidal et al., 2017*).
813 However, our study showed that significant matrix porosity and permeability
814 enhancement can occur with alterations in some parts of the DZ, and more
815 significantly in fractured clusters and fault cores. This is confirmed by the comparison
816 between our models from the outcrop and the URG wells, even if the secondary
817 mineralization linked to hydrothermal flows present in the URG are not observed on
818 outcropping shoulders. This suggests that fracture clusters and FZ in the basement
819 reservoirs can offer suitable volume for flow storage and circulation within the rock
820 mass, in addition to the connected fracture network.
821 The study presented here is a first step for the characterization of the matrix
822 properties in fault zones of the WER. Combined to an extensive study of the fracture
823 network, these data can supply dual porosity modelling and help prediction of the
824 actual fluid flows in the basement of the grabens.
825
826
827
828 Glossary:
829
830 DZ: Damage Zone
831
832 CdF: Champ-du-Feu
833
834 FC: Fault Core
835
836 FZ: Fault Zone
837
838 FMC: French Massif Central
839

k: Permeability

LLFZ: Lalaye-Lubine Fault Zone

TC: Thermal Conductivity

Vp: P-Waves Velocity

WER: West European Rift

WL: Weathered Layer

Appendix A: synthesis of the petrographic and petrophysical evolution in fault zones for group I rock facies: ferromagnesian minerals and plagioclase/feldspar alteration degree, microcrack densities on thin sections, measured porosity, permeability, Vp and TC ranges and example of PPL and CPL view.

Group	Classification (Nb of samples)	Ferromagnesian minerals alteration	Feldspar - plagioclases alteration	Microcracks density	Porosity (H_2O & Hg) (%)	k (m^2)	Vp ($km.s^{-1}$)	TC ($W.m^{-1}.K^{-1}$)	PPL	CPL
I : granites and granodiorites	Fresh (35)	-	-	-	0 to 3	1.10^{-19} to 4.10^{-16}	3.0 to 5.4	2.3 to 3.0	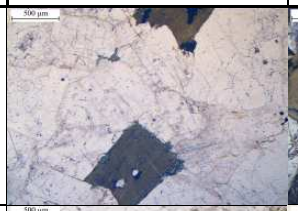	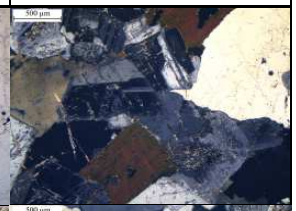
	Weakly altered (21)	+	+	-	1 to 4	2.10^{-18} to 7.10^{-15}	2.1 to 4.4	2.1 to 3.0	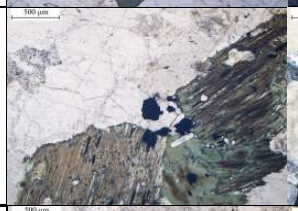	
	DZ samples : moderately altered (8)	++	++	-/+	4 to 11	6.10^{-18} to 2.10^{-13}	1.9 to 4.0	1.7 to 2.8	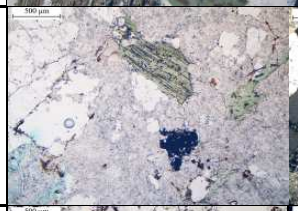	
	FC samples (15)	+++	+++	++	5 to 52	2.10^{-15} to 4.10^{-14}	2.7 to 3.7	2.2 to 2.8	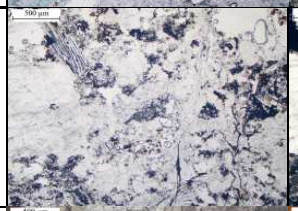	
	Saprolite (11)	+	+	+++	4 to 33		1.7 to 3.4	0.7 to 2.0	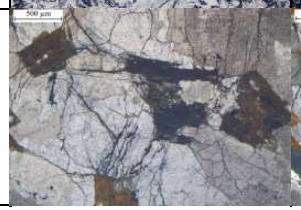	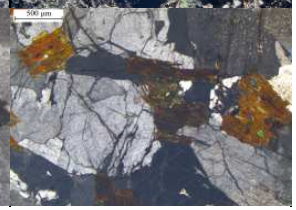

Appendix B: synthesis of the petrographic and petrophysical evolution in fault zones for group II rock facies: ferromagnesian minerals and plagioclase/feldspar alteration degree, microcracks density on thin sections, measured porosity, permeability, Vp and TC ranges and example of PPL and CPL view.

Group	Classification (Nb of samples)	Ferromagnesian minerals alteration	Feldspar - plagioclases alteration	Microcracks density	Porosity (H_2O & Hg) (%)	k (m^2)	Vp ($km.s^{-1}$)	TC ($W.m^{-1}.K^{-1}$)	PPL	CPL
II : main metamorphic units	Coarse-grained fresh (8)	-	-	-	0 to 4	2.10^{-19} to 2.10^{-18}	4.2 to 5.2	2.3 to 3.8		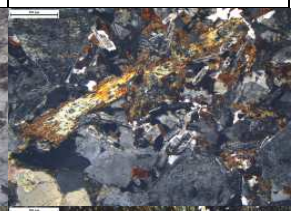
	Fine-grained fresh (15)	-	-	+	0 to 10	1.10^{-19} to 4.10^{-15}	3.3 to 5.7	2.2 to 4.8		
	Coarse-grained altered (10)	+	+	-	1 to 7	1.10^{-18} to 3.10^{-15}	2.9 to 5.5	1.9 to 3.2		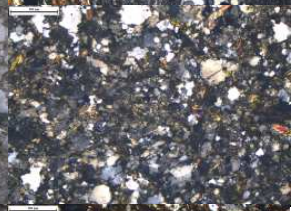
	fine-grained altered (22)	+	+	++	1 to 13	2.10^{-18} to 5.10^{-16}	2.8 to 6.0	1.3 to 5.0		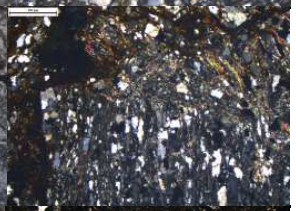
	FC samples (6)	+	+	++	8 - 42	$< 5.10^{-15}$	2.5 to 3.2	2.0 to 3.6	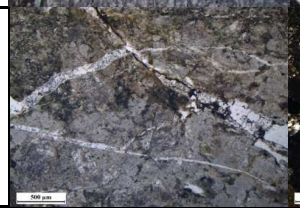	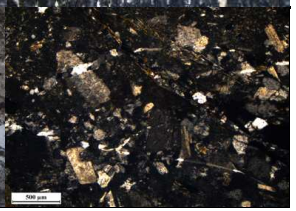

Appendix C: synthesis of the petrographic and petrophysical evolution in fault zones for group I rock facies: ferromagnesian minerals and plagioclase/feldspar alteration degree, microcracks density on thin sections, measured porosity, permeability, Vp and TC ranges and example of PPL and CPL view.

Group	Classification (Nb of samples)	Ferromagnesian minerals alteration	Feldspar - plagioclases alteration	Microcracks density	Porosity (H_2O & Hg) (%)	k (m^2)	Vp ($km.s^{-1}$)	TC ($W.m^{-1}.K^{-1}$)	PPL	CPL
III : massive rocks	Fresh - Migmatites (2)	-	-	+	0 to 2	4.10^{-17} to $.10^{-17}$	2.4 to 3.0	2.4 to 2.7		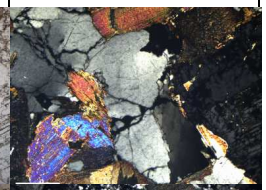
	Altered Migmatites (3)	+	+	+	3 to 6	1.10^{-17} to 2.10^{-15}	1.3 to 4.3	2.2 to 2.7	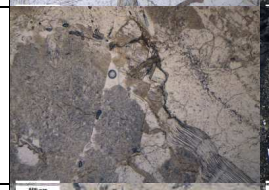	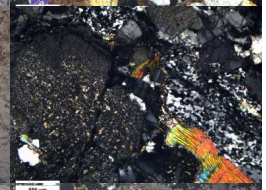
	Schirmeck massif & Southern unit (17)	+	+	+/-	0 to 3	2.10^{-18} to 6.10^{-15}	1.6 to 6.0	2.3 to 3.7		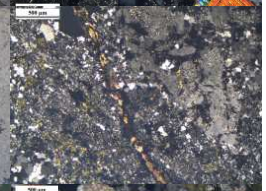
	Fresh diorites (10)	-	-	+/-	0 to 2	3.10^{-19} to 2.10^{-18}	3.2 to 5.7	2.2 to 2.8	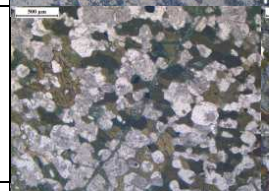	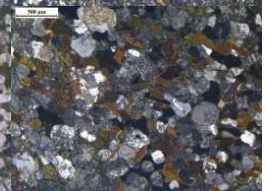
	Altered diorites (4)	+	+	+/-	1 to 5	9.10^{-18} to 4.10^{-17}	2.2 to 5.5	2.1 to 2.3	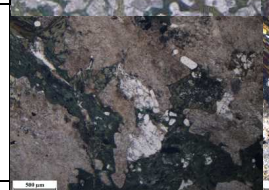	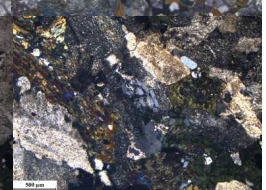
	FC - samples (5)	++	++	++	5 - 15	-	-	-		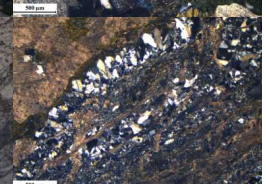

Acknowledgements

This work was supported by Fonroche Geothermie industry and University of Lorraine with GeoRessources laboratory. It is also a part of the REFLET project funded by the GIS Geodenergies. The authors would also like to thank the helpful comments received by the two anonymous reviewers and associate editor Dr. Eva Schill.

References:

Areshev, E.G., Dong, T.L., San, N.T., Shnip, O.A., 1992. Reservoirs in fractured basement on the continental shelf of southern Vietnam. Journal of Petroleum Geology, 15, n°4, 451–464. doi:10.1111/j.1747-5457.1992.tb01045.x.

Baillieux, P., 2012. Multidisciplininary approach to understand the localization of geothermal anomalies in the Upper Rhine Graben regional to local scale. University of Neuchâtel, Phd Thesis, 131 p.

Barbarin, B., Gagny, C., Jeambrun, M., Didier, J., Pellaton, C., Delfour, J., Leistel, J.-M., 1988. Carte géologique de Noiretablee. BRGM geological map n°695, scale 1:50,000.

Bauer, J.F., Krumbholz, M., Meier, S., Tanner, D.C., 2017. Predictability of properties of a fractured geothermal reservoir: the opportunities and limitations of an outcrop analogue study. Geothermal Energy, 5:24. Doi:10.1186/s40517-017-0081-0.

Beach, A., Welbon, A.I., Brockbank, P.J., McCallum, J.E., 1999. Reservoir damage around faults: outcrop examples from the Suez Rift. Petroleum Geoscience, 5, 109–116.

Belikov, B.P., 1967. Plastic constants of rock-forming minerals and their effect on the elasticity of rocks. Physical and mechanical properties of rocks. Academy of Sciences of the USSR, Israel Program for Scientific Translations, Jerusalem, 124-140.

Bense, V.F., Gleeson, T., Loveless, S.E., Bour, O., Scibek, J., 2013. Fault zone hydrogeology. Earth-Science Reviews, 127, 171-192.

Bertrand, L., Jussaume, J., Géraud, Y., Diraison, M., Damy, P.C., Navelot, V., Haffen, S., 2018. Structural heritage, reactivation and distribution of fault and fracture network in a rifting context: Case study of the western shoulder of the Upper Rhine Graben. Journal of Structural Geology, 108, 243-255.

Blanalt, J.G., von Eller, J.P., Fluck, P., Geffroy, J., Jeannette, D., Ruhland, M., Schwoerer, P., Thevenin, A., Stieber, A., Vogt, H., 1972. Carte géologique de Sélestat. BRGM geological map n°307, scale 1:50,000.

Boissavy, C., Henry, L., Genter, Pomart, A., Rocher, P., Schmidlé-Bloch, V., 2019. Geothermal Energy Use, Country Update for France. European Geothermal Congress 2019, The Hague, The Netherlands, 11-14 June, 1-18.

Bornand, M., Mandier, P., Monjuvent, G., Chenevoy, M., Combier, J., 1977. Notice explicative de la carte géologique de France, Feuille Valence, n°818, édition Bureau des Ressources Géologiques et Minières, 54p.

Bouiller, R., Giot, D., Jeambrun, M., Scanvic, P., 1976. Carte géologique de Thiers. BRGM geological map n°694, scale 1:50,000.

Bouiller, R., Baras, L., 1978. Carte géologique de Le Mayet-de-Montagne. BRGM geological map n°671, scale 1:50,000.

Boulanouar, A., Rahmouni, A., Boukalouch, M., Samaouali, A., Géraud, Y., Harnafi, M., Sebbani, J., 2013. Determination of thermal conductivity and porosity of building stone from ultrasonic velocity measurements. Geomaterials, 03, 138–144.

Bourgeois, O., Ford, M., Diraison, M., Le Carlier de Veslud, C., Gerbault., M., Pik, Ruby, N., Bonnet, S., 2007. Separation of tifting and lithospheric folding signatures in the NW-Alpine foreland. International Journal of Earth Sciences, 96, 1003-1031.

Bourquin, S., Peron, S., Durand, M., 2006. Lower Triassic sequence stratigraphy of the western part of the Germanic Basin (west of Black Forest): Fluvial system evolution through time and space. Sedimentary Geology, 186, 187-211.

Boutin, R., Montigny, R., Thuizat, R., 1995. Chronologie K-Ar et ^{39}Ar-^{40}Ar du métamorphisme et du magmatisme des Vosges. Comparaison avec les massifs varisques voisins. Géologie de la France, 1, 3-25.

Bruguier, O., Becq-Giraudon, J.F., Bosch, D., Lancelot, J.-R., 1998. Late Visean (upper Missisipian) hidden basins in the internal zones of the Variscan Belt: U-Pb zircon evidence from the French Massif Central. Geology, 26, 627-630.

Brun, J.P., Gutscher, M.A., DEKORP-ECORS teams, 1992. Deep crustal structure of the Rhine Graben from DEKORP-ECORS seismic reflection data: a summary. Tectonophysics, 208, 139-147.

Burg, J.-P., Leyreloup, A., Marchand, J., Matte, P., 1984. Inverted metamorphic zonation and large-scale thrusting in the Variscan belt: an example in the French Massif Central. In: Hutton, D.H.W., Sanderson, D.J., Variscan Tectonics of the North- Atlantic Region. Geological Society of London, Special Publication, 14, 47–61.

Burg, J.P., Delor, C., Leyreloup, A., Romney, F., 1989. Inverted metamorphic zonation and Variscan thrust tectonics in the Rouergue area (Massif Central, France): P – T – t record from mineral to regional scale. In: Daly, J.S., Cliff, R.A., Yardley, B.W.D., Evolution of Metamorphic Belts. Geological Society of London, Special Publications, 439, 423 – 439.

Caine, J.S., Evans, J.P., Forster, C.B., 1996. Fault zone architecture and permeability structure. Geology, 24, 1025-1028.

Carpentier, S., Steeghs, P., Boxem, T., 2016. Seismic reprocessing and attributes for geothermal exploration: a case study in Friesland, Netherlands. European Geothermal Congress, Strasbourg, France, 19-24 septembre, 1-8.

Cello, G., Tondi, E., Micarelli, L., Invernizzi, C., 2001. Fault zone fabrics and geofluid properties as indicators of rock deformation modes. Journal of Geodynamics, 32, 543–565.

Čermák, V., Rybach, L., 1982. Thermal conductivity and specific heat of minerals and rocks. In: Landolt and Börnstein V/1: Physical properties, G. Angenheister Ed., Springer, 305-344.

Chenevoy, M., Lorenchet de Montjamont, M., Gros, J.-J., 1976. Carte géologique de Crest. BRGM geological map n°842, scale 1:50,000.

Dadet, P., Léopold; C., Régis, Fleury, R., Jeambrun, M., Giot, D., 1980. Carte géologique de Maringues. BRGM geological map n°670, scale 1:50,000.

Darot, M., Reuschlé, T., 2000. Acoustic wave velocity and permeability evolution during pressure cycles on a thermally cracked granite. International Journal of Rock Mechanics & Mining Sciences, 37, 1019-1026.

Debrand-Passard, S., Courbouleix, S., Lienhardt, M.-J., 1984. Synthèse géologique du Sud-Est de la France. Mémoire du Bureau des Ressources Géologiques et Minières, 125, 618 p.

De Joussineau, G., Aydin, A., 2007. The evolution of damage zone with fault growth in sandstone and its multiscale characteristics. Journal of Geophysical Research, 112, B12401.

Dewandel, B., Lachassagne, P., Wyns, R., Maréchal, J.C., Krishnamurthy, N.S., 2006. A generalized 3-D geological and hydrogeological conceptual model of granite aquifers controlled by single or multiphase weathering. Journal of Hydrology, 330, 260– 284.

Edel, J.-B., Schulmann, K., Rotstein, Y., 2007. The Variscan tectonic inheritance of the Upper Rhine Graben: evidence of reactivations in the Lias, Late Eocene–Oligocene up to the recent. International Journal of Earth Science, 96, 305-325.

Elsass, P., von Eller, J.P., Stussi, J.M., 2008. Géologie du massif du Champ du Feu et de ses abords. Eléments de notice pour la feuille géologique 307 Sélestat. Rapport BRGM RP-56088-FR.

Esteban, L., Pimienta, L., Sarout, J., Delle Piane, C., Haffen, S., Géraud, Y., Timms, N.E., 2015. Study cases of thermal conductivity prediction from P-wave velocity and porosity. Geothermics, 53, 255–269.

Faulkner, D.R., Jackson, C.A.L., Lunn, R.J., Schlische, R.W., Shipton, Z.K., Wibberley, C.A.J., Withjack, M.O., 2010. A review of recent developments

concerning the structure, mechanics and fluid flow properties of fault zones. Journal of Structural Geology, 32, 1557-1575.

Faure, F., Monié, P., Pin, C., Maluski, H., Leloix, C., 2002. Late Visean thermal event in the northern part of the French Massif Central: new $^{40}Ar/^{39}Ar$ and Rb-Sr isotopic constraints on the Hercynian syn-orogenic extension. International Journal of Earth Sciences, 91, 53-75.

Faure, M., B. Mézème, E., Cocherie, A., Rossi, P., Chemenda, A., Boutelier, D., 2008. Devonian geodynamic evolution of the Variscan Belt, insights from the French Massif Central and Massif Armoricain. Tectonics, 27, TC002115.

Faure, M., Lardeaux, J. M., Ledru, P., 2009. A review of the pre-Permian geology of the Variscan French Massif Central. Comptes-Rendus Geosciences, 341, 202–213.

Freymark, J., Sippel, J., Scheck-Wenderoth, M., Bär, K., Stiller, M., Fritsche, J.G., Kracht, M., 2017. The deep thermal field of the Upper Rhine Graben. Tectonophysics, 694, 114-129.

Genter, A., Guillou-Frottier, L., Breton, J.P., Denis, L., Dezayes, Ch., Egal, E., Feybesse, J.L., Goyeneche, O., Nicol, N., Quesnel, F., Quinquis, J.P., Roig, J.Y., Schwartz, S., 2004. Typologie des systèmes géothermiques HDR-HFR en Europe, Rapport Bureau des Ressources Géologiques et Minières, RP-53452-FR, 165 p.

Genter, A., Giot, D., Lieutenant, N., Nehlig, P., Rocher, Ph., Roig, J.Y., Chevremont, P., Guillou-Frottier, L., Martelet, G., Bitri, A., Perrin, J., Serrano, O., Courtois, N., Vigourous, Ph., Negrel, P., Serra, H., Petelet-Giraud, E., Brach, M., Calcagno, P. Courrioux, G., Goyeneche, O., 2003. Méthodologie de l'inventaire du potentiel géothermique des Limagnes : projet COPGEN. Rapport d'avancement. RP-52643-FR, 31 p.

Géraud, Y., Rosener, M., Surma, F., Place, J., Le Garzic, E., Diraison, M., 2010. Physical properties of fault zones within a granite body: Example of the Soultz-sous-Forêts geothermal site. Comptes-Rendus Geoscience, 342, 566–574.

Giot, D., Alsac, C., Jeambrun, M., 1986. Carte géologique d'Aiqueperse. BRGM geological map n°669, scale 1:50,000.

Glaas, C., Genter, A., Girard, J.F., Patrier, P., Vidal, J., 2018. How do the geological and geophysical signatures of permeable fractures in granitic basement evolve after long periods of natural circulation? Insights from the Rittershoffen geothermal wells (France). Geothermal Energy, 6:14. Doi: 10.1186/s40517-018-0100-9.

Gros, J.-J., Benkö, D., Mandier, P., Chenevoy, M., Monjuvent, G., Lorenchet de Montjamont, M., 1977. Carte géologique de Valence. BRGM geological map n°818, scale 1 :50,000.

Guillocheau, F., Robin, C., Allemand, P., Bourquin, S., Brault, N., Dromart, G., Friedenberg, R., Garcia, J.-P., Gaulier, J.-M., Gaumet, F., Grosdoy, B., Hanot, F., Le Strat, P., Mettraux, M., Nalpas, T., Prijac, C., Rigollet, C., Serrano, O., Grandjean, G.,

2000. Meso-Cenozoic geodynamic evolution of the Paris basin: 3D stratigraphic constraints. Geodynamica Acta 13, 189–245.

Gutmanis, J.C., Bachelor, T., Doe, S., Pascual-Cebrian, E., 2015. Hydrocarbon production from fractured basement formations. Public report, version 11, p.45.

Haffen, S., Géraud, Y., Rosener, M., Diraison, M., 2017. Thermal conductivity and porosity maps for different materials: A combined case study of granite and sandstone. Geothermics, 66, 143-150.

Hettkamp, T., Fuhrmann, G., Rummel, F, 1999. Hydraulic properties in the rhine graben basement material. Bulletin d'Hydrogéologie, n°17, 143–50.

Jeambrun, M., Giot, D., Bouiller, R., 1973. Carte géologique de Clermont-Ferrand. BRGM geological map n°693, scale 1:50,000.

Khair, H.A., Cooke, D., Hand, M., 2015. Seismic Mapping and Geomechanical Analyses of Faults within Deep Hot Granites, a Workflow for Enhanced Geothermal System Projects. Geothermics, 53, 46-56.

Klinkenberg, L.J., 1941. The Permeability of Porous Media to Liquids and Gases. Presented at the Drilling and Production Practice. American Petroleum Institute.

Koning, T., 2013. Fractured and Weathered Basement Reservoirs: Best Practices for Exploration and Production – Examples from USA, Venezuela and Brazil. Search and Discovery, 41250, p. 29.

Kranz, R.L., Frankel, A.D., Engelder, T., Scholz, C.H., 1979. The Permeability of Whole and Jointed Barre Granite. International Journal of Rock Mechanics and Mining Sciences, 16, 225-234.

Kushnir, A. R.L., Heap, M.J., Gilg, H.A., Reuschlé, T., 2018. Characterizing the physical properties of rocks from the Paleozoic to Permo - Triassic transition in the Upper Rhine Graben. Geothermal Energy, 6:16. Doi:10.1186/s40517-018-0103-6

Lardeaux, J.M., Schulmann, K., Faure, M., Janouš̆k, V., Lexa, O., Skrzypek, E., Edel, J.B., Štípská P., 2014. The Moldanubian Zone in the French Massif Central, Vosges/Schwarzwald and Bohemian Massif revisited: differences and similarities. In: Schulmann, K., Martinez, Catalan, J.R., Lardeaux, J.M., Janouš̆k, V., Oggiano, G. (eds) 2014. The Variscan Orogeny: Extent, Timescale and the Formation of the European Crust. Geological Society, London, Special Publications, 405, 7–44.

Ledésert, B., Hebert, R., Genter, A., Bartier, D., Clauer, N., 2010. Fractures, hydrothermal alterations and permeability in the Soultz Enhanced Geothermal System. Comptes-Rendus Geoscience, 342, 607-615.

Ledru, P., Courrioux, G., Dallain, C., Lardeaux, J.M., Montel, J.M., Vanderhaeghe, O., Vitel, G., 2001. The Velay dome (French Massif Central): melt generation and granite emplacement during orogenic evolution. Tectonophysics, 342, 207-237.

Matte P., 2001. The Variscan collage and orogeny (480 ± 290 Ma) and the tectonic definition of the Armorica microplate: a review. Terra Nova, 13, 122-128.

Montjuvent, G., Chenevoy, M., Mandier, P., 1979. Carte géologique de Tournon. BRGM geological map n°794, scale 1:50,000.

Morrow, C., Lockner, D., Hickman, S., Rusanov, M., Röckel T., 1994. Effects of lithology and depth on the permeability of core samples from the Kola and KTB drill holes. USGS Staff - Published Research, Paper 408, 7263-7274.

Morrow, C.A., 2000. Permeability of Deep Drillhole Core Samples. Proceedings, International Workshop on the Nojima Fault Core and Borehole Data Analysis, Nov. 22-23, 1999, Tsukuba, Japan. edited by H. Ito, K. Fujimoto, H. Tanaka and D. Lockner, 2000.

Menillet, F., Durand, M., Maïaux, C., Lougnon, J., 1978. Carte géologique de Cirey-sur-Vezouze. BRGM geological map n°270, scale 1:50,000.

Mielke, P., Bär, K., Sass, I., 2017. Determining the relationship of thermal conductivity and compressional wave velocity of common rock types as a basis for reservoir characterization. Journal of Applied Geophysics, 140, 135–144.

Mitchell, T.M., Faulkner, D.R., 2009. The nature and origin of off-fault damage surrounding strike-slip fault zones with a wide range of displacements: a field study from the Atacama fault system, northern Chile. Journal of Structural Geology, 31, 802–816.

Nance, R.D., Gutiérrez-Alonso, G., Keppie, J.D., Linnemann, U., Murphy, J.B., Quesada, C., Strachan, R.A., Woodcock, N.H., 2010. Evolution of the Rheic Ocean. Gondwana Research, 17, 194–222.

Nelson, R.A., 2001. Geological Analysis of Naturally Fractured Reservoirs, Second ed. Gulf Professional Publishing, p. 332.

Olivet, J.L., 1996. Kinematics of the Iberian plate. Bulletin des Centres de Recherches Exploration-Production Elf Aquitaine, 131-195.

Pirajno, F., 2009. Hydrothermal Processes and Mineral Systems. Edition Springer, 1250 p.

Popov, Y., A., Pribnow, Dan F.C., Sassc, J.H., Williams, C.F., Burkhardt, H., 1999. Characterization of rock thermal conductivity by high-resolution optical scanning. Geothermics, 28, 253-276.

Rosener, M., 2007. Etude pétrophysique et modélisation des effets des transferts thermiques entre roche et fluide dans le contexte géothermique de Soultz-sous-Forêts. University Strasbourg 1, PhD thesis, 204 p.

Rosener, M., Géraud, Y., 2007. Using physical properties to understand the porosity network geometry evolution in gradually altered granites in damage zones. Geological Society, London, Special Publications, 284, 175-184.

Roussé, S., 2006. Architecture et dynamique des series marines et continentals de l'Oligocène Moyen et Supérieur du Sud du Fossé Rhénan: Evolution des milieux de depôt en contexte de rift en marge de l'avant-pays alpin. Strasbourg University, Phd Thesis, 483 p.

Schumacher, M.E., 2002. Upper Rhine Graben: Role of preexisting structures during rift evolution. Tectonics, 21, n° 1. doi: 10.1029/2001TC900022.

Sissingh, W., 2001. Tectonostratigraphy of the West Alpine Foreland: correlation of Tertiary sedimentary sequences, changes in eustatic sea-level and stress regimes. Tectonophysics, 333, 361–400.

Skrzypek, E., 2011. Contribution structurale, pétrologique et géochronologique à la tectonique intracontinentale de la chaîne hercynienne d'Europe (Sudètes, Vosges). PhD Thesis, Strasbourg University, 412 p.

Skrzypek, E., Schulmann, K., Tabaud ,A.S., Edel, J.B., 2014. Palaeozoic evolution of the Variscan Vosges Mountains. In: Schulmann, K., Martinez Catalan, J.R., Lardeaux, J.M., Janoušĕk, V., Oggiano, G. (eds) 2014. The Variscan Orogeny: Extent, Timescale and the Formation of the European Crust. Geological Society, London, Special Publications, 405, 7–44. doi:10.1144/SP405.8.

Slightam, C., 2014. Characterizing seismic-scale faults pre- and post-drilling; Lewisian Basement, West of Shetlands, UK. In : Spence, G. H., Redfern, J., Aguilera, R., Bevan, T. G., Cosgrove, J. W., Couples, G. D. & Daniel, J.-M. (eds) 2014. Advances in the Study of Fractured Reservoirs. Geological Society, London, Special Publications, 374, 311–331. http://dx.doi.org/10.1144/SP374.6

Srivastava, S., Roest, W.R., Kovacs, L.C., Schouten, H., Kligord, K., 1990. Iberian plate kinematics: A jumping plate boundary between Eurasia and Africa. Nature, 344, 756- 759.

Stober I., Bucher K., 2007. Hydraulic properties of the crystalline basement. Hydrogeology Journal, 15, 213-224.

Surma, F., Géraud, Y., 2003. Porosity and thermal conductivity of the Soultz-sous-Forêts granite. Pure and Applied Geophyics, 160, 1125–1136.

Tabaud, A.S., 2012. Le magmatisme des Vosges: conséquence des subductions paléozoïques, (datation, pétrologie, géochimie, ASM). Strasbourg university, Phd thesis, 227 p.

Tabaud, A.S., Whitechurch, H., Rossi, P., Schulmann, K., Guerrot, C., Cocherie, A., 2014. Devonian-Permian magmatic pulses in the northern Vosges Mountains (NE France): result of continuous subduction of the Rhenohercynien Ocean and Avalonian passive margin. In: Schulmann K., Martinez Catalan J.R., Lardeaux J.M., Janoušĕk

V., Oggiano G. (eds) 2014. The Variscan Orogeny: Extent, Timescale and the Formation of the European Crust. Geological Society, London, Special Publications, 405, 7–44.

Theobald, N., Menillet, F., Vogt, H., Thevenin, A., Schwoerer, P., Lougnon, J., 1975. Carte géologique de Molsheim. BRGM geological map n°271, scale 1:50,000.

Trice, R., 2014. Basement exploration, West of Shetlands: progress in opening a new play on the UKCS. Geological Society of London, Special Publications, 397, 81–105.

Velde, B.B., Meunier, A., 2008. The Origin of Clay Minerals in Soils and Weathered Rocks. Springer Science & Business Media Edition, 406 p.

Vidal, J., Genter, A., Schmittbuhl, J., 2016. Pre- and post-stimulation characterization of geothermal well GRT-1, Rittershoffen, France: insights from acoustic image logs of hard fractured rock. Geophysical Journal International, 206, 845–860.

Vidal, J., Genter, A., and Chopin, F., 2017. Permeable fracture zones in the hard rocks of the geothermal reservoir at Rittershoffen, France. Journal of Geophysical Research: Solid Earth, 122, 4864– 4887. doi:10.1002/2017JB014331.

Vidal, J., Genter, A., 2018. Overview of naturally permeable fractured reservoirs in the central and southern Upper Rhine Graben: Insights from geothermal wells. Geothermics, 74, 57–73.

von Eller, J.P., Menillet, F., Hollinger, J., Guillaume, C., Billoret, R., Fluck, P., Maïaux, C., 1975. Carte géologique de Saint-Dié. BRGM geological map n°306, scale 1:50,000.

Weinert, S., Baer, K., Sass, I., 2020. Thermophysical rock properties of the crystalline Gonghe Basin Complex (Northeastern Qinghai–Tibet-Plateau, China) basement rocks. Environmental Earth Sciences, 79, 77. doi: 10.1007/s12665-020-8808-9.

Wilmarth, M., Stimac, J., 2015. Power Density in Geothermal Fields. Proceedings World Geothermal Congress, Melbourne, Australia, 19-25 avril, 1-7.

Ziegler, P.A., Schumacher, M.E., Dezes, P., Van Wees, J.D., Cloetingh, S., 2006. Post-Variscan evolution of the lithosphere in the area of the European Cenozoic Rift System. Geological Society, London, Memoirs, 32, 97-112.